We are IntechOpen,
the world's leading publisher of
Open Access books
Built by scientists, for scientists

4,800
Open access books available

122,000
International authors and editors

135M
Downloads

154
Countries delivered to

Our authors are among the

TOP 1%
most cited scientists

12.2%
Contributors from top 500 universities

BOOK CITATION INDEX
CLARIVATE ANALYTICS
INDEXED

WEB OF SCIENCE™

Selection of our books indexed in the Book Citation Index
in Web of Science™ Core Collection (BKCI)

Interested in publishing with us?
Contact book.department@intechopen.com

Numbers displayed above are based on latest data collected.
For more information visit www.intechopen.com

5

Physical Deposition Assisted Colloidal Lithography: A Technique to Ordered Micro/Nanostructured Arrays

Yue Li[1,3], Shuyan Gao[2], Guotao Duan[1], Naoto Koshizaki[3] and Weiping Cai[1]
[1]Key Laboratory of Materials Physics, Institute of Solid State Physics,
Chinese Academy of Sciences, Anhui,
[2]College of Chemistry and Environmental Science, Henan Normal University, Xinxiang
[3]Nanosystem Research Institute (NRI) National Institute of Advanced Industrial Science
and Technology (AIST)
[1,2]China
[3]Japan

1. Introduction

Ordered micro/nanostructured arrays have attracted much interest due to their important applications in microfluidic devices, optoelectronic devices, nanophotonics, field emitters, nanogenerators, sensors, nano-biotechnology, surface science, photocatalytic properties etc.[1-11] The traditional routes to create periodic micro/nanostructured arrays are generally divided into two step. Microsized structure arrays are first fabricated by traditional lithographic techniques (e.g. photo-lithography, electron-beam lithography, ion beam lithography, x-ray lithography)[12-15] as well as soft lithography (e.g. the techniques of replica molding, microcontact printing, micromolding in capillaries)[16-19], the nanostructures are then modified on the microsized units in array,[20] thus hierarchical micro/nanostructured arrays are finally achieved. However, they cannot be afforded due to the high costs and time-consuming in the most laboratories. Recently, the monolayered colloidal crystals (or called colloidal monolayers), ordered monolayer colloidal sphere arrays with hexagonal close-packed lattice structures on a certain substrate by self-assembly,[21-35] can be used to prepare ordered structure arrays. [36-41] It has proved that it is a flexible approach to fabricate the periodic micro or nanostructure arrays (e.g. nanoparticle arrays,[42-49] nanopore arrays,[50-59] hollow sphere arrays[60-65]) based on colloidal monolayer templates by the different routes, solution/sol-dipping route, electrochemical deposition etc. Their properties are morphology and arrangement parameter dependent. Besides these periodic structure arrays, the colloidal monolayer template also can be used to prepare hierarchical micro/nanostructured arrays. For example, the hierarchical micro/nanostructured polystyrene (PS) sphere/CNTs composite arrays were obtained by wet chemical self assembling;[66-68] hierarchical microsized PS sphere/silver nanoparticle composite arrays or microsized pore/silver nanoparticle arrays were made by thermal deposition of silver precursor;[69,70] gold hierarchical micro/nanostructured particle arrays were created by electrochemical deposition based two step replication of colloidal monolayer template.[71] However, these routes have been

developed by basically chemical reaction. They have some disadvantages of impurities on surface of arrays due to incompletely   decomposition of precursors, residua of surfactants in self-assembling or electrochemical deposition. Additionally, it is quite difficult to achieve very uniform morphology of hierarchical micro/nanostructure arrays on a large-scale. Another route of colloidal monolayer template combining with physical deposition is expected to resolve these problems. In this chapter, we focus on introducing the recent work to create micro/nanostructured arrays based on colloidal templates with physical deposition (pulsed laser deposition (PLD) and sputtering). The parameters of microstructure or nanostructure can be tuned by periodicities of colloidal templates or experimental conditions of physical deposition. The applications of nanorod arrays with controllable morphology and arrangement parameters in self-cleaning surfaces, enhanced catalytic properties, field emitters etc. are also presented in following section.

2. Pulsed laser deposition assisted colloidal lithography[73,74]

2.1 Method

A polystyrene (PS) colloidal monolayer was first fabricated on a substrate. The desired material was then deposited on this colloidal monolayer substrate by PLD at room temperature and oxygen was introduced into PLD chamber as the background gas. This periodic array has a special hierarchical micro/nanostructure array with a hexagonal-close-packed (hcp) arrangement, which originate from the pattern of colloidal monolayer. In this micro/nanostructure unit in array, the nanorod stands vertically on the microsized PS sphere tops, and nanobranches in each nanorod grow in a radiationlike manner, perpendicular to the PS sphere surface. The detailed experiments are described as following.
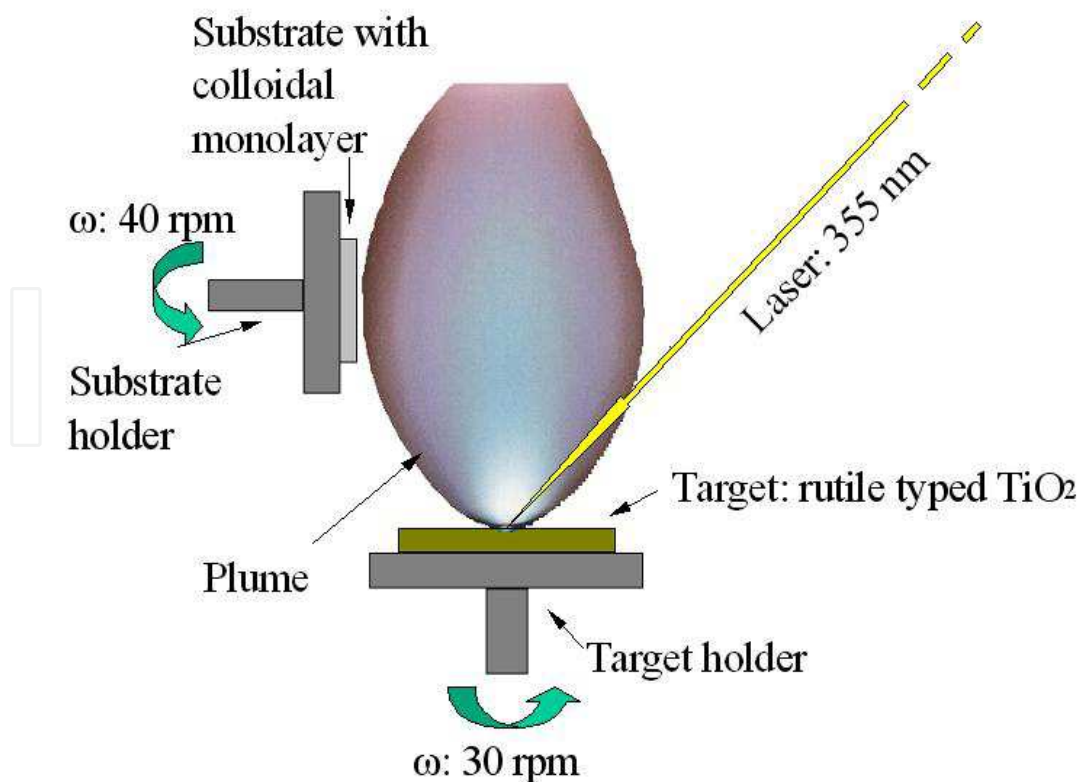

Fig. 1. Schematic illustration of PLD process.

Commercial monodispersed PS spheres dispersed in water with a certain size were purchased from companies. The PS colloidal monolayers were first fabricated on cleaned Si substrates by self-assembly using spin coating. The colloidal monolayer with its supporting substrate was placed in a deposition chamber of PLD, close to the target and at an off-axial position with respect to the target, as shown in Figure 1.A laser beam with a 355 nm wavelength from a Q-switched Nd:YAG laser (Continuum, Precision 8000), operated at 10 Hz with 100 mJ/pulse and a pulse width of 7 ns was applied and focused on the target surface with a diameter of about 2 mm. The desired target, for example, rutile typed titanium dioxide was used for deposition. The substrate and target were rotated at 40 and 30 rpm, respectively. PLD was carried out at a base pressure of 2.66×10^{-4} Pa and a background O_2 pressure of 6.7 Pa.
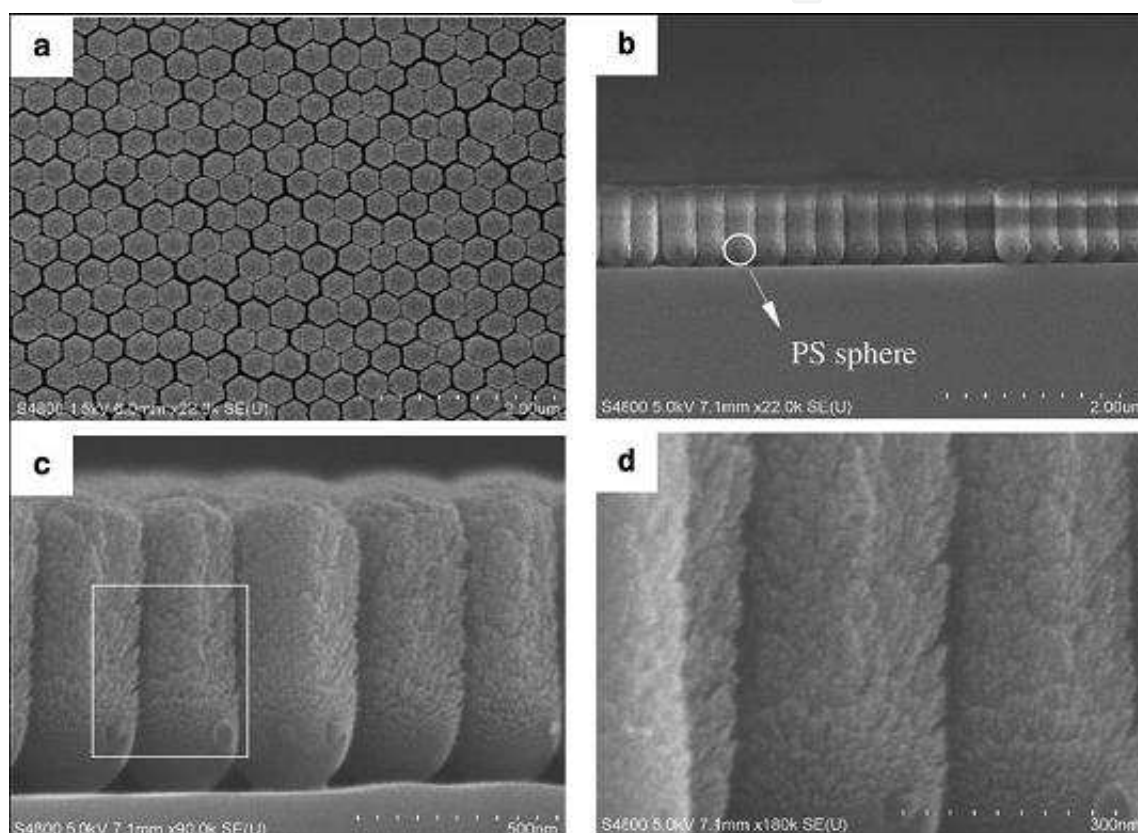

Fig. 2. Morphology of a sample obtained by PLD using a Si substrate with a PS colloidal monolayer coating (PS sphere size: 350 nm; deposition time: 70 min). (a) FESEM image from top view and (b) FE-SEM image of cross-section. (c) and (d) are high-resolution images observed from the side. (d) much higher magnification image of (c).

After deposition, the sample demonstrated a periodic hierarchical micro/nanorod array with an hcp arrangement, as reflected from Figure 2a. Each nanorod consists of two parts: a PS sphere at the bottom and a vertical nanorod on the top of the PS sphere (Figure 2b). The diameter of the nanocolumn was almost the same as that of the PS sphere, 350 nm, and its height was about 870 nm. The nanorod had a very rough structure on the surface and was composed of many nanobranches, according to the high-resolution images of the side view (Figure 2 c, d). TEM observation from the top of the nanorod arrays reflects that each nanorod consists of radiation-shaped nanobranches emanating from the center (Figure 3a).
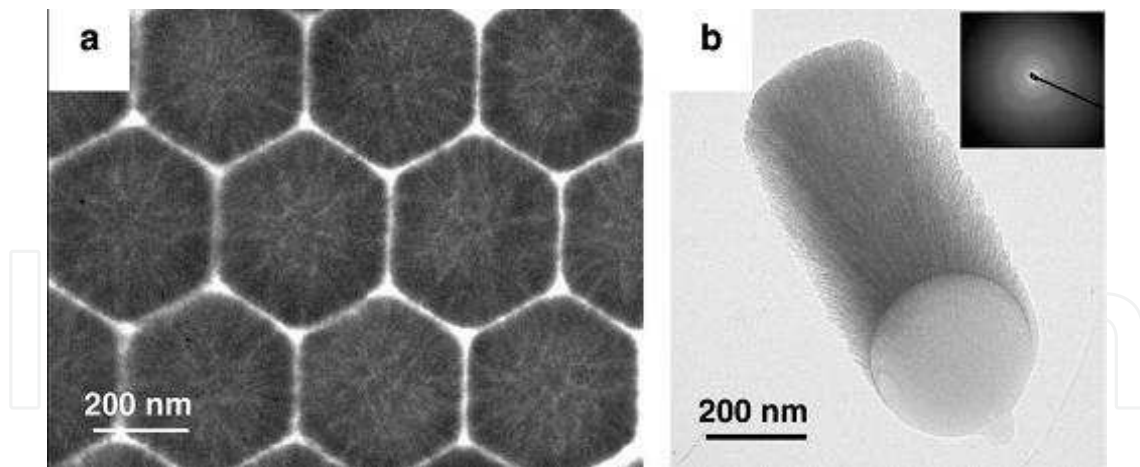
Fig. 3. Corresponding TEM images of the sample in Figure 2. (a) Periodic nanorod array observed from the top. (b) Single nanorod observed from the side. The inset in (b) is the corresponding electron diffraction pattern.
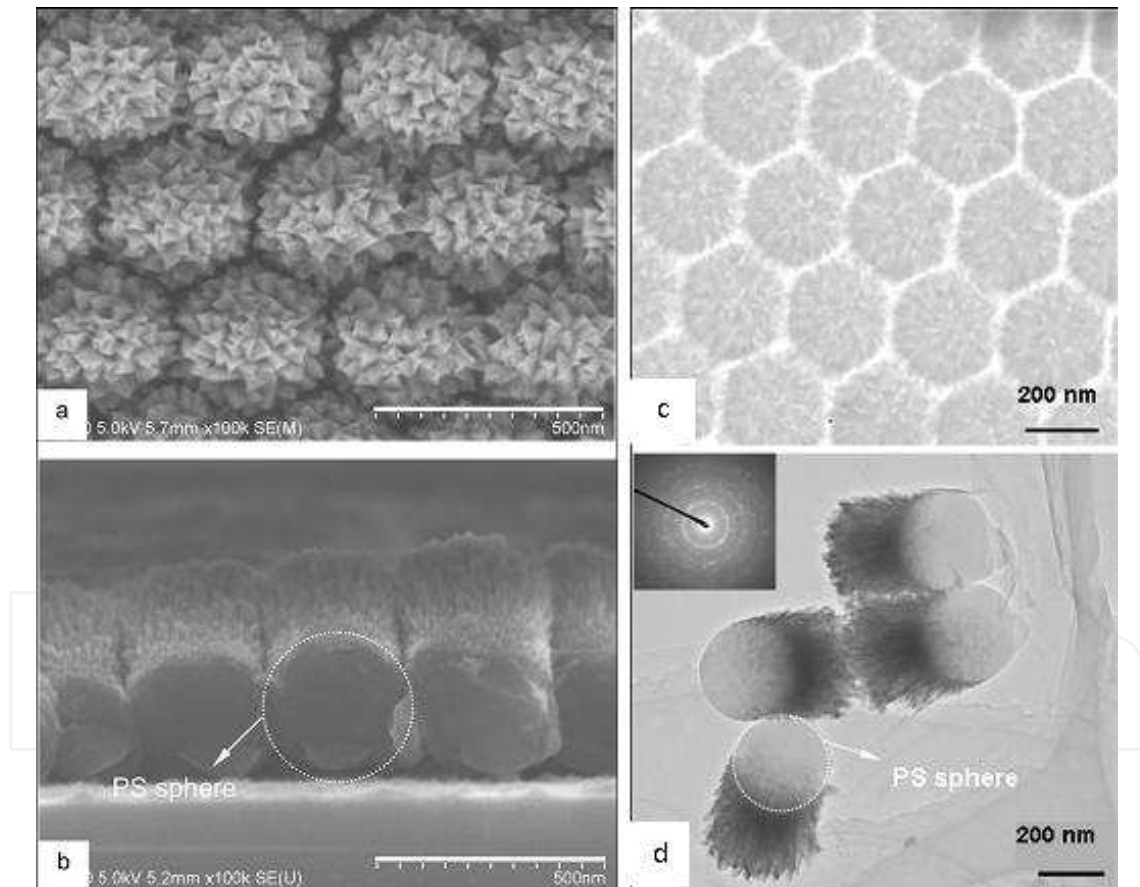

Fig. 4. a, b: FE-SEM images of a CuO hierarchical micro/nanostructured array obtained by combining the PS colloidal monolayer and PLD process. (PS sphere size 350 nm, deposition time 2 h, ambient oxygen pressure during deposition 6.7 Pa). (a) top-view image; (b) section view. Scale bars in parts a and b indicate 500 nm. c, d: TEM images of a CuO hierarchical micro/nanostructured array: (c) TEM image from the top; (d) TEM image of several separated units from the periodic array and the corresponding selected area electron diffraction (SAED) pattern.

The TEM image of a single nanorod also clearly displays that the nanorod consists of a PS sphere at bottom and a nanocolumn on the sphere surface. The nanorod possesses nanobranch-structures, which grow almost vertically on the PS sphere surface (Figure 3b). The nanobranch-structures indicate that the nanorod has a hierarchical, porous structure and hence has a high surface area. The selected area electron diffraction (SAED) pattern shows that the deposited materials on PS sphere surfaces by PLD are amorphous. Besides TiO_2 amorphous hcp nanocolumn arrays, the presented strategy can be extended to the fabrication of similar amorphous structures of SnO_2, WO_3, C, and so forth, just by changing the corresponding target in the PLD process.

Additionally, some materials, e.g. CuO, Fe_2O_3, ZnO are easily crystalline by PLD at room temperature. If the colloidal monolayer is applied as a template, the crystalline CuO, Fe_2O_3, ZnO etc. hierarchical micro/nanostructured arrays can be also obtained. Figure 4 shows the SEM and TEM image CuO crystalline hierarchical micro/nanostructured arrays using colloidal monolayers as templates by PLD. Each arrayed unit is composed of PS sphere at bottom and deposited materials at top. Deposited materials are well crystalline, they do not exhibit round shapes but radially aligned nanocolumns having tips with trigonal pyramidal shapes on the PS sphere.

The deposited CuO nanostructures can be tuned by varying ambient gas pressures during the PLD process. Figure 5 shows the FE-SEM and TEM images of samples achieved by PLD under higher ambient gas pressures during the PLD process using the colloidal monolayers as substrates. When oxygen pressure increased from 6.7 to 26.7 Pa, the morphology did not appreciably change and exhibited similar hierarchical structures as before (Figure 5a). However, when the oxygen pressure increased to 53.3 Pa, the morphology completely changed and was very different from those at lower pressures. The nanocolumn tips on the PS sphere demonstrated imperfect trigonal pyramid shapes, and the tip sizes became much smaller (Figure 5b). According to the corresponding TEM image and SAED pattern (Figure 5c), we find that hierarchical micro-/nanostructures were still observed at such high oxygen pressure, but the crystallization of deposited aligned nanocolumns on the PS sphere becomes worse than that obtained at lower oxygen pressure. When the gas pressure increased to as high as 79.8 Pa, similar hierarchical micro-/nanostructured array was not obtained, and many aggregates of small particles were produced on the colloidal monolayer template (Figure 5d). The XRD spectra of the samples obtained under different oxygen pressures are shown in Figure 6. Strong preferential orientation growth along (002) was observed at the gas pressure of 26.7 Pa. Increasing oxygen pressure led to weakening of this preferential orientation and broadening of X-ray diffraction peaks. This result reflects that deposited materials gradually changed to small nanoparticles from aligned nanocolumn arrays and the particles became much smaller with increasing oxygen pressure during PLD, agreeing with FE-SEM images. When the oxygen pressure increased to very high value, 79.8 Pa, the deposited material completely consisted of small nanoparticles or the aggregates of small nanoparticles, and there was no preferential orientation growth. Because when the gas pressure increases to a high value, the plume is compressed into a smaller space in PLD process, and the possibility of collision among ions or atoms in plasma is greatly enhanced, further resulting in a kinetic energy decrease of ions or atoms, which leads to less crystallization and smaller nanoparticle formation[75].
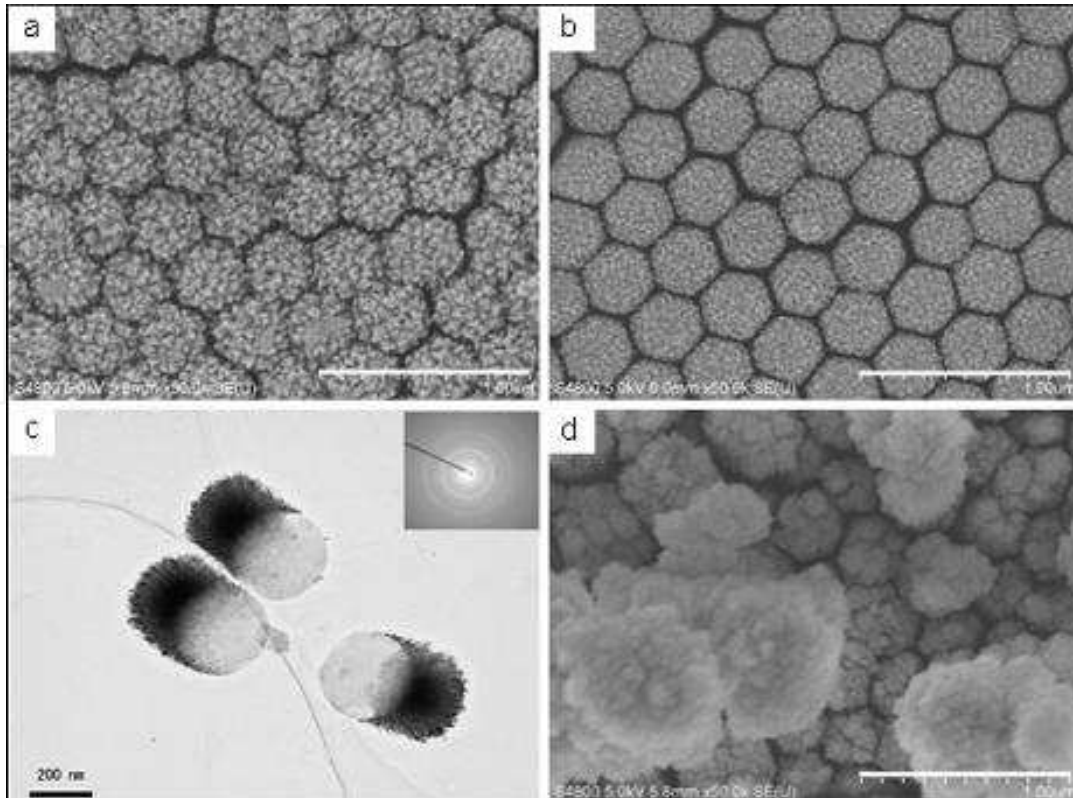
Fig. 5. Images obtained by the different ambient oxygen pressures: (a, b, d) FE-SEM images of the samples obtained under ambient oxygen pressure of 26.7, 53.3, and 79.8 Pa, respectively; (c) TEM image of the sample obtained at 53.3 Pa and the corresponding SAED pattern of several units. Scale bars in (a), (b), and (d): 1 μm.
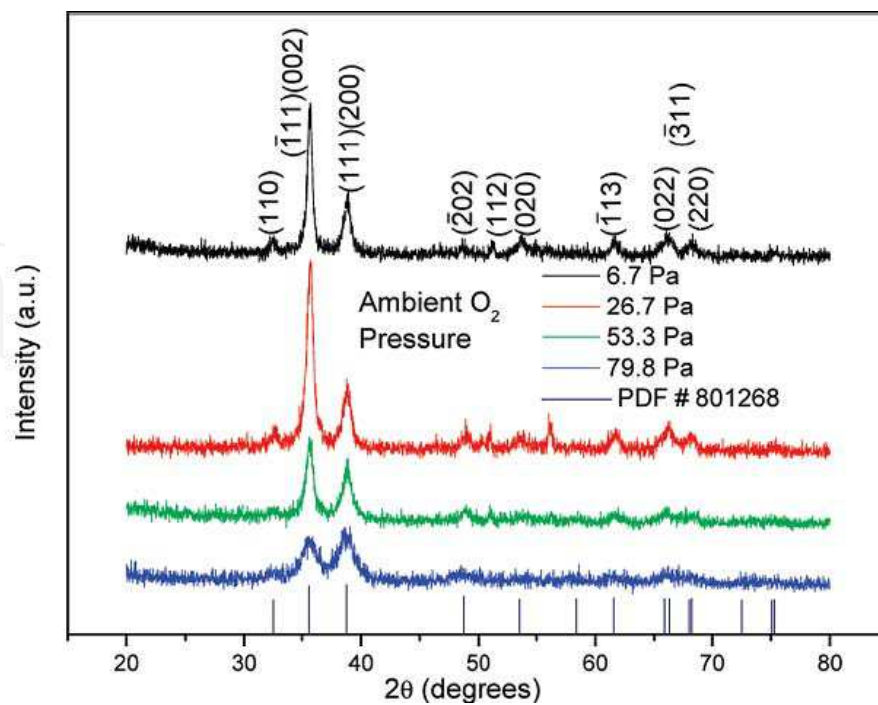

Fig. 6. XRD patterns of the samples obtained under different oxygen pressures.

Similar crystalline hierarchical micro-/nanostructured arrays of Fe_2O_3 and ZnO can be also created by the same route, as shown in Figure 7. Fe_2O_3 nanobelts or ZnO nanocolumns were well aligned on the PS sphere tops, like those of CuO. However, the Fe_2O_3 nanobelt or ZnO nanocolumn tops were not like those of CuO. The slight differences among CuO, Fe_2O_3, and ZnO fine nanostructures are determined mainly by their various chemical and physical properties: a crystal facet of the interface with different energies etc.
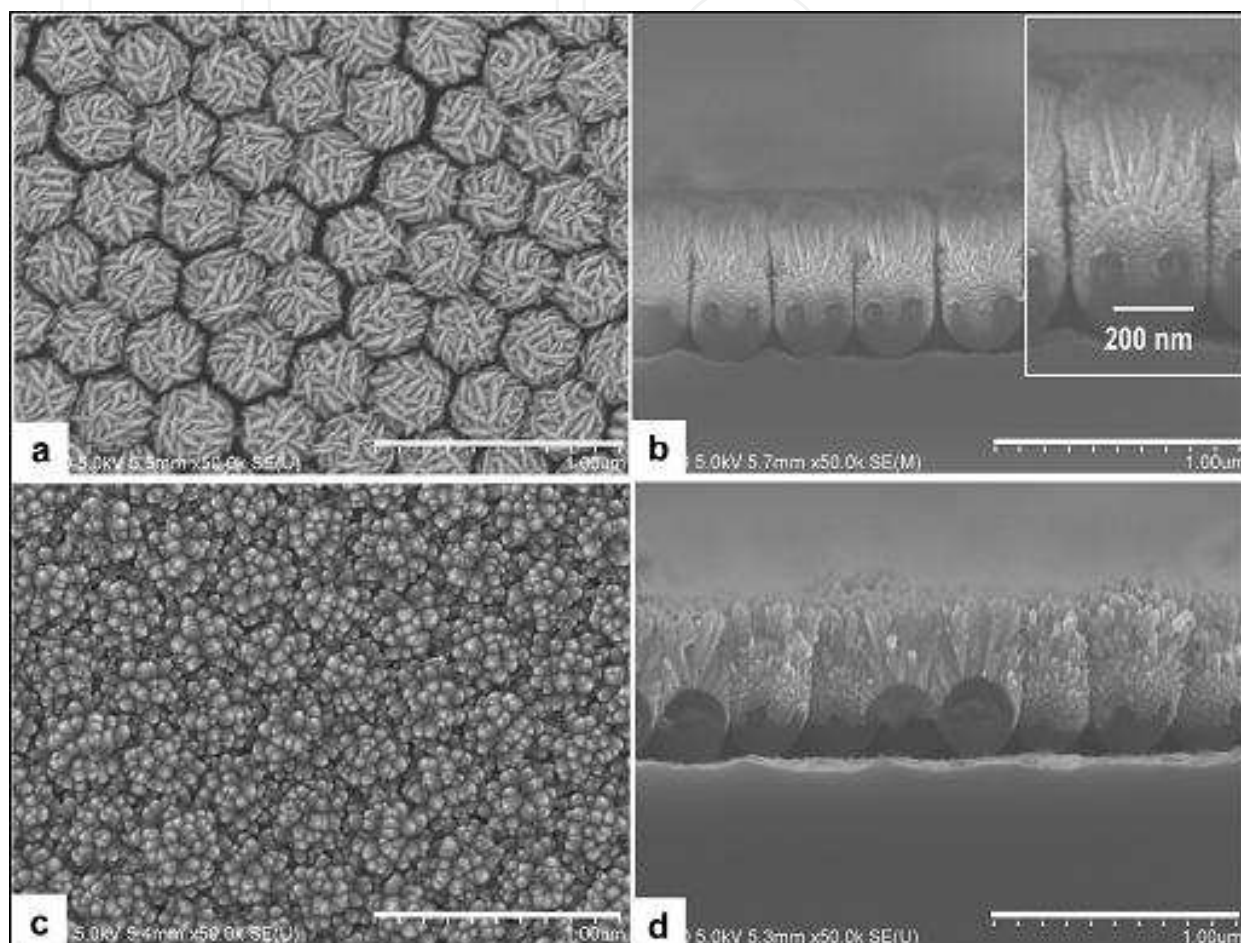
Fig. 7. FE-SEM images of hierarchical micro-/nanostructured arrays of Fe_2O_3 and ZnO. (a, b) Fe_2O_3, oxygen pressure 6.7 Pa, deposition time 1.5 h; (c, d) ZnO. a and c: top views; b and d: side views (oxygen pressure 6.7 Pa and deposition 40 min). The inset in (b): the high magnification image of a single Fe_2O_3 hierarchical micro-/ nanostructure.

In this strategy, the height of micro/nanostructured unit can be obviously controlled by varying deposition time during PLD process, the height will increase with increase of PLD time. From the Figure 8, it can be found that the unit height increases by increasing deposition time from 30 min to 60 min. However, if the deposition time is too long, to say, 180 min, the tops of micor/nanostructured units will aggregate with each other due to strong Van de Waals attraction among units in the deposition process, as shown in Figure 8 (c), (c') and (c''). Additionally, the top of micro/nanostructured unit gradually flattens from convex shape with increasing deposition time, resulting in a weakening shadow effect. Therefore, a continuous film might be formed at top of hierarchical micro/nanostructured array if further increasing deposition time after 180 min.
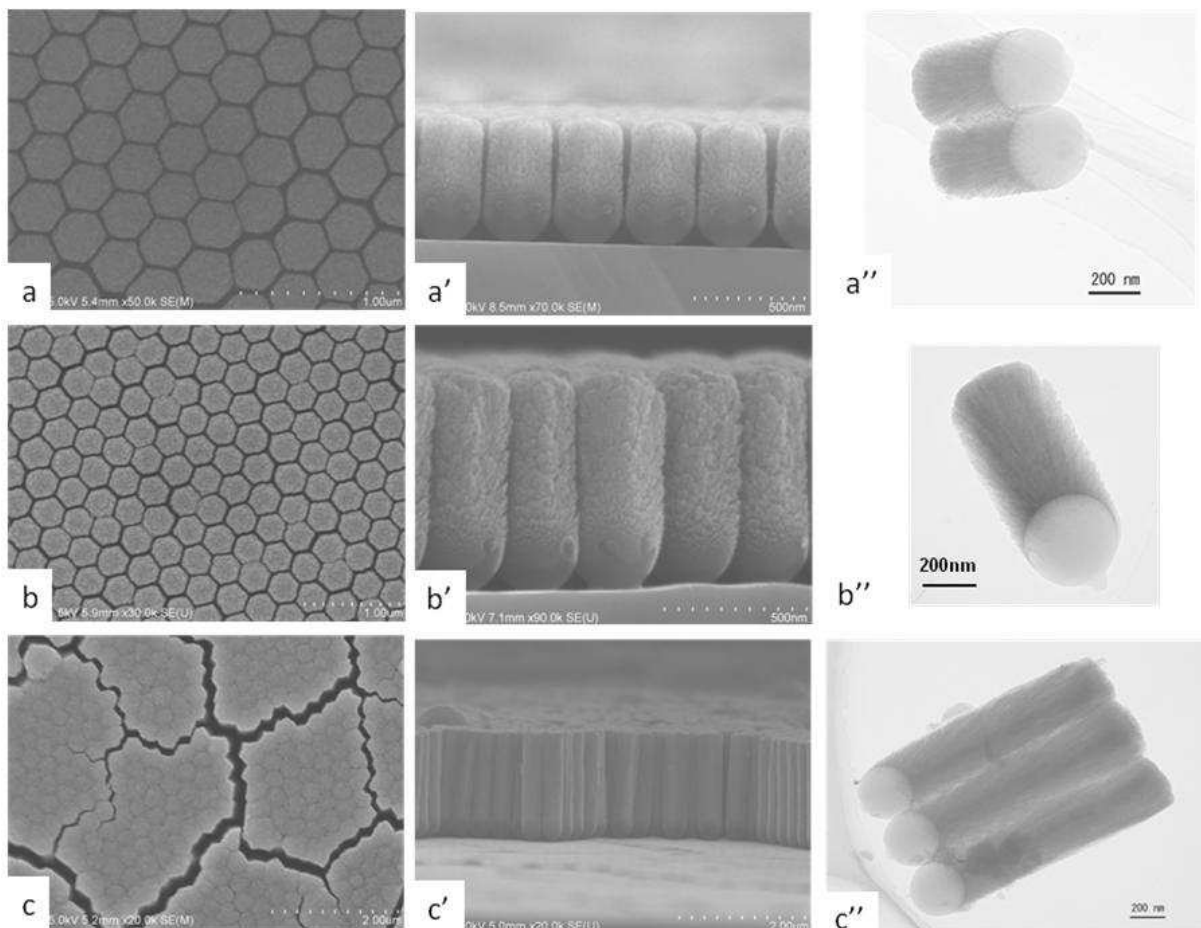
Fig. 8. The height changes of micro/nanostructured unit with increase deposition time. Deposition time: 30 min in (a), (a′) and (a′′); 60 min in (b), (b′) and (b′′); 180 min in (c), (c′) and (c′′). (a), (b) and (c) are SEM images of top view; (a′), (b′) and (c′) are SEM images of cross-section; (a′′), (b′′) and (c′′) are TEM images of micro/nanostructure units.

The as-prepared hierarchical micro/nanostructured units in periodic arrays are composed of a PS sphere at the bottom and a micro/nano- particle or rod on the top of the PS sphere. If the PS colloidal template is dissolved by an organic solution (CH_2Cl_2), this periodic array could retain its integrity while being peeled from the substrate due to the van der Waals force between the neighboring micro/nanostructured units suspended in the solution. It could then be transferred to any desired substrate (e.g., TEM copper grid) by picking it up using another substrate, as illustrated in Figure 9 and Figure 10. The transferability avoids restrictions on substrates in the fabrication process of hierarchical micro/nanostructured arrays, which is helpful in the design and fabrication of new micro-/nano- devices on any desired substrates.
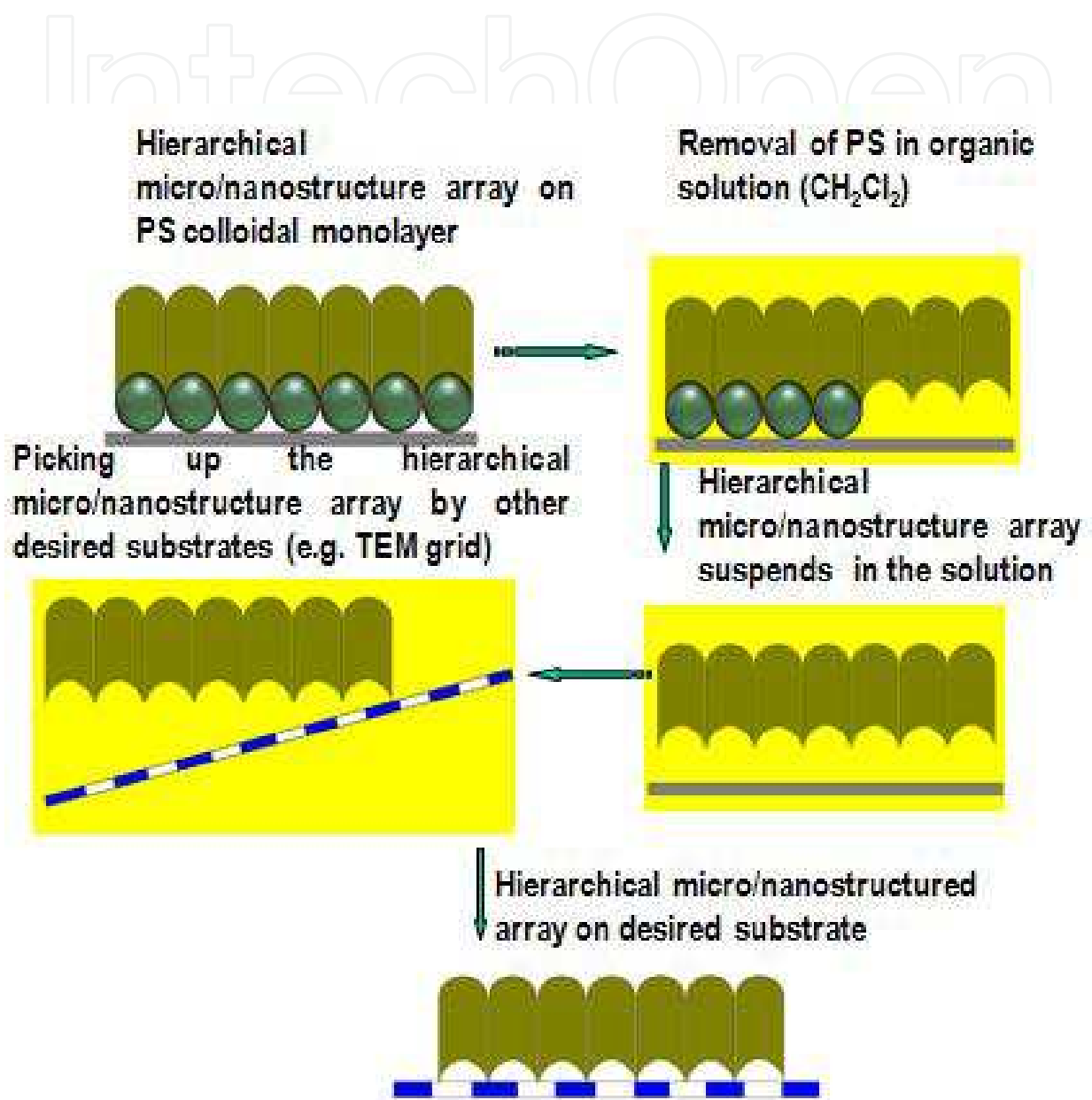
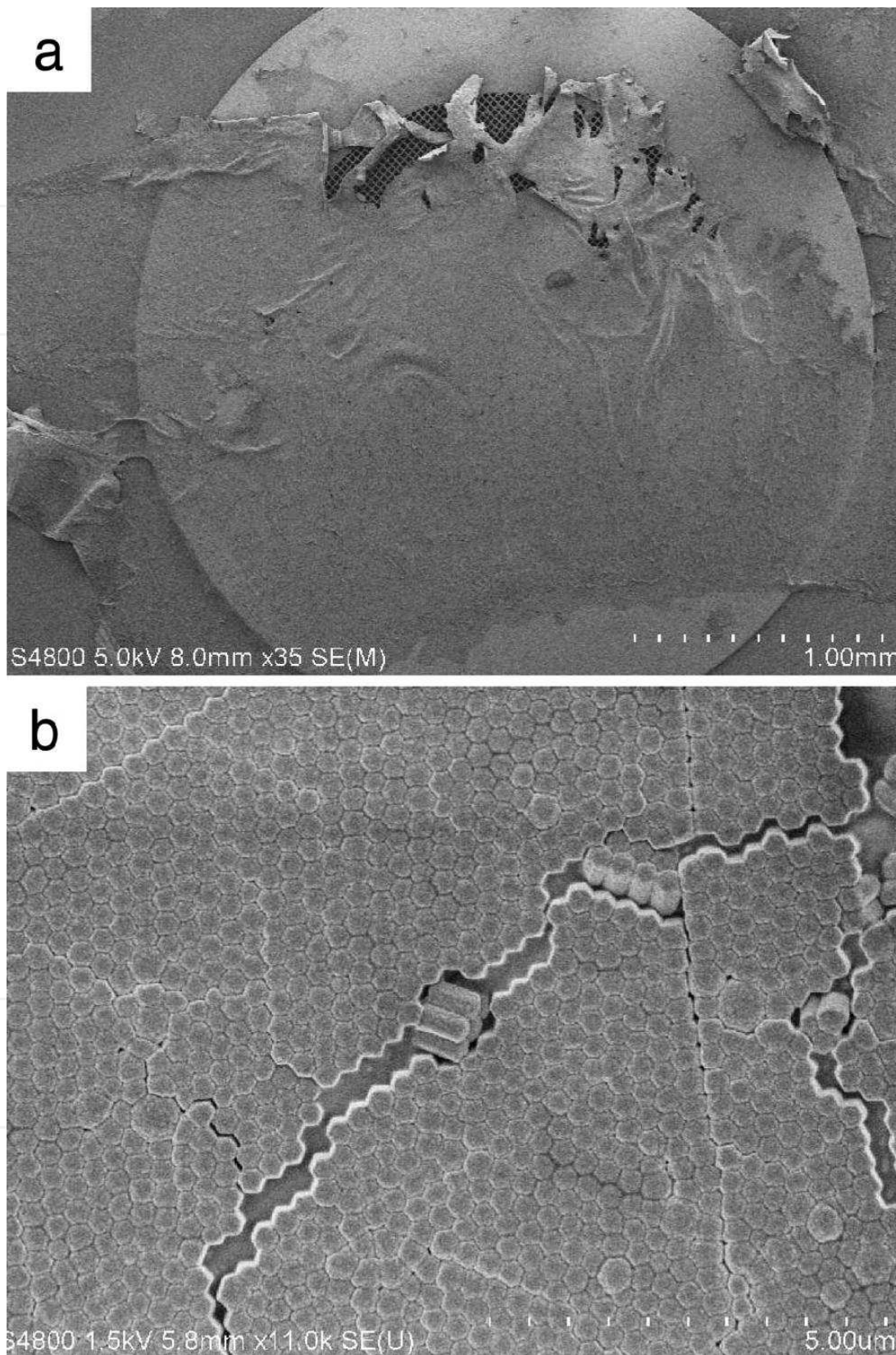Fig. 9. Schematic illustration of transferability of hcp hierarchical micro/nanostructured arrays

Fig. 10. FE-SEM images of transferred TiO₂ micro/nanostructured arrays from a silicon substrate on a TEM grid. (a) Low- and (b) high-magnification images of array film on a TEM grid.

2.2 Formation mechanism of hierarchical micro/nanostructured arrays by PLD

The formation process was traced by PLD using colloidal clusters with different PS spheres as templates. Herein, the TiO_2 was selected as desired material and colloidal monolayer with PS sphere size of 350 nm as template to demonstrate the formation process of hierarchical micro/nanostructured arrays. The colloidal clusters with different PS sphere were fabricated by spin-coating with a higher rotation speed (2000 rpm) and lower concentration (1.0 wt%) of PS colloidal microsphere suspension. For example, a single PS sphere or PS sphere clusters with different sphere numbers (2, 3, 4,...) can be easily created on the substrate by above route, as indicated in column A of Table 1. After PLD, morphologies observed from the top compared to those before PLD, as demonstrated in column B of Table 1. For a single PS microsphere, the shape kept spherical but that the size increased from 350 nm (PS sphere size) to 500 nm after PLD. For the PS sphere-clusters with sphere number from two to six, each unit size in the sphere-cluster still increased, but could not maintain the spherical shape after PLD. Growth of deposited TiO_2 was restricted at the contact point of two neighboring PS spheres, the contact between the neighboring units changed from a quasidot contact to a facet contact before (PS sphere-cluster) and after (PS sphere-cluster with deposited materials on the surface) PLD. If a PS sphere in sphere-cluster was completely surrounded by others, e.g., the central sphere in a hexagonal close packed (hcp) sphere-cluster of seven, its size after deposition was almost the same as before PLD and the morphology was slightly changed from spherical shape to hexagonal one. A section of a PS sphere-cluster of 10 spheres with hcp arrangement after PLD displays that hierarchical micro/nanorods have formed on the two spheres completely surrounded by the others and that hierarchical rod cannot be formed on the spheres at the edge of the sphere-cluster. This implies that a hierarchical micro/nanostructured array will be easily produced after PLD if a colloidal monolayer with a large-scale is applied in the PLD process. Additionally, if the desired materials are deposited on a bare silicon substrate without any PS spheres by PLD, nanocolumns grow vertically on the Si substrate, as seen in Figure 11.

Generally, nanocolumns prefer to grow in the normal direction on the substrate during the PLD process.[75] In the PLD process, the desired target (TiO_2) is irradiated by a laser beam using an energy level exceeding its threshold in vacuum environment, plasma including ions (Ti^{4+}, O^{2-}, etc.), molecules, electrons and clusters are released into the PLD chamber from the target. However, if a background gas with high pressure is introduced into the chamber, the movement direction of ions or electrons will be changed from an almost uniform direction to multidirection due to collisions between the ions, electrons, molecules and clusters of the ejected species and the background gas. According to the above facts, the formation mechanism of hierarchical hcp nanocolumn arrays can be easily understood, as displayed in Figure 12. If a substrate without PS spheres is used in the PLD process, a film consisting of vertical nanocolumns of small diameter will be formed. If a single PS sphere exists on the substrate, a composite of a PS sphere at the bottom and a shell composed of TiO_2 radiation-shaped nanobranches on sphere top will turn up, due to preferential vertical growth along the normal direction of the supporting surface and multidirectional deposition. For a PS sphere cluster (more than one sphere) on the substrate, a shadow effect will be produced in the deposition between any two neighboring spheres. If one sphere in the sphere-cluster is completely surrounded by six other spheres as in the case of hcp arrangement, one rod with hierarchical micro/nanostructure will grow on this sphere top. If a colloidal monolayer with a large scale is adopted, this route can easily fabricate an hcp hierarchical micro/nanostructured array. In this strategy, an off-axis configuration is adopted where the target and substrate are perpendicularly placed. It is similar to the glancing angle deposition (GLAD) or oblique angle deposition in which there is a large

angle between the deposition direction and the normal direction of the substrate.[76-84] In the traditional GLAD method, atoms from the target obliquely arrive and condense on the substrate, and the tilted and separated nanowire or nanopillar array with a porous structure are gradually produced due to the shadow effect of the initial deposited nanoparticles under high-vacuum conditions. The critical difference between this route and GLAD is the background gas pressure during deposition, which converts the directional flow of ejected species in a vacuum into a multidirectional one at higher pressure. Therefore, this multidirection deposition and shadow effect are a principal reason why a vertical hierarchical micro/nanostructured array with hcp alignment is formed on the colloidal monolayer. This can be further verified by varying the angles between substrates and target in PLD process, as seen in Figure 13 and 14. If these experiments were carried out in a vacuum, tilted rod-like structured arrays with different angles would be obtained on the different substrates. However, from these results, the rod-like morphologies are independent of the angle between the substrate and target but the growth rates are different for different angles because of the plume shape in PLD , they always grow vertically on the substrate due the multiple direction deposition combined with shadow effect of neighboring colloidal sphere (Figure 14).
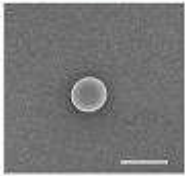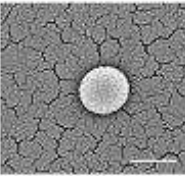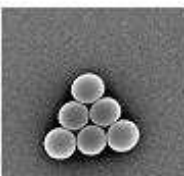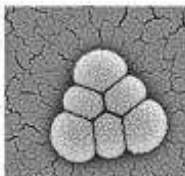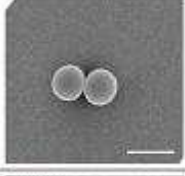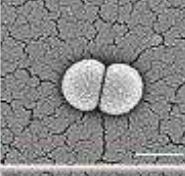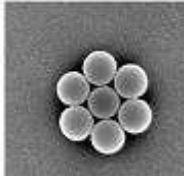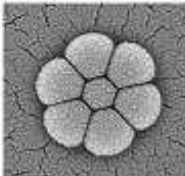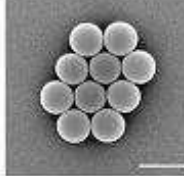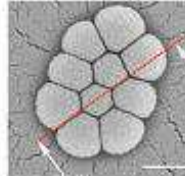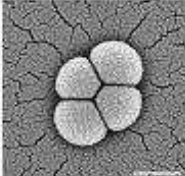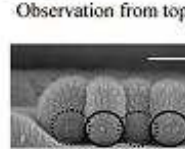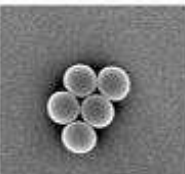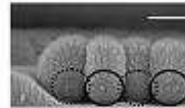

Table 1. Morphologies of before and after PLD on the PS sphere surface (Scale bars are 500 nm)
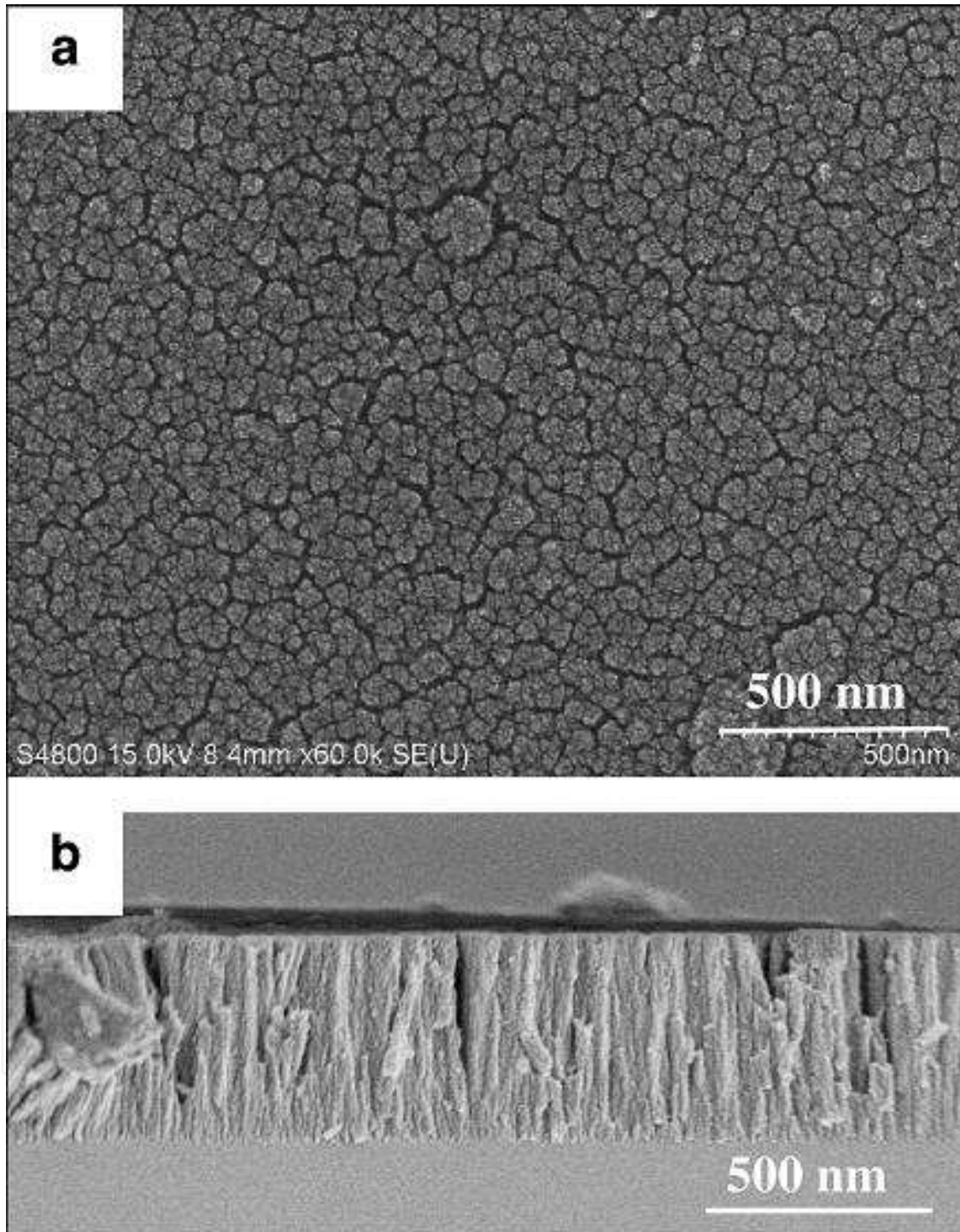
Fig. 11. FE-SEM images of the TiO$_2$ nanocolumns deposited by PLD directly on a bare substrate without colloidal spheres. (a) Observation from top. (b) Section view.
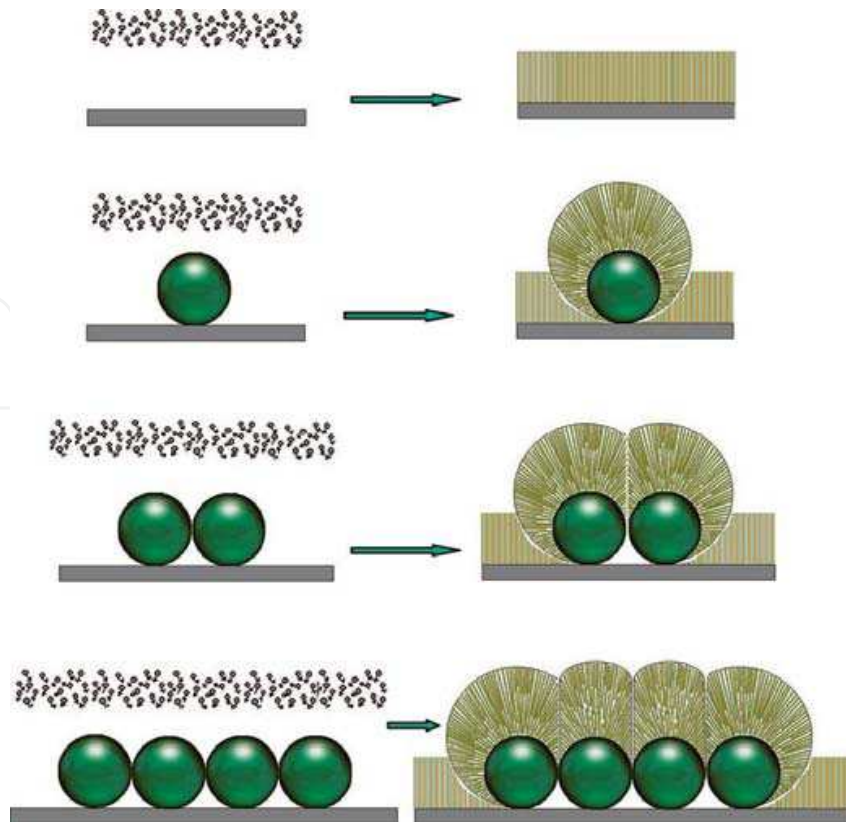
Fig. 12. Schematic illustration of formation mechanism of hcp hierarchical micro/nanostructured arrays.
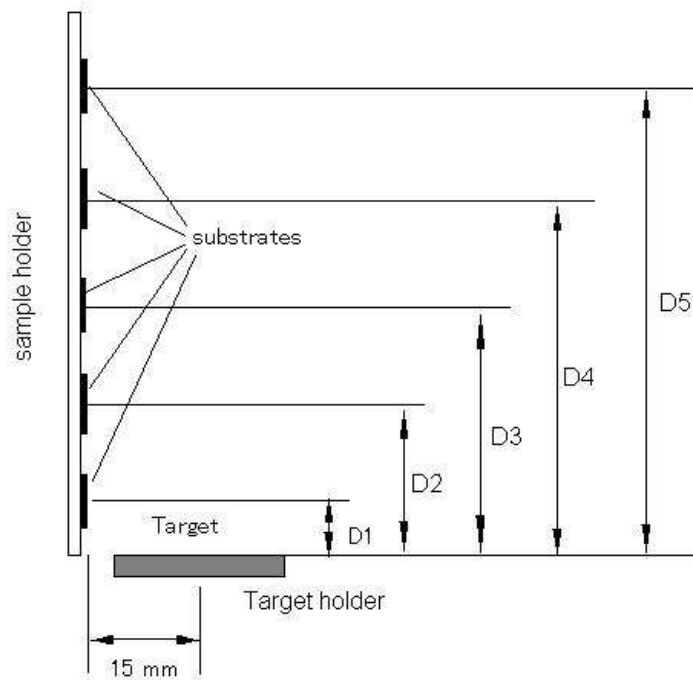
Fig. 13. Schematic illustration of multi-substrate experiment. D1: 8 mm. D2: 23 mm. D3: 35 mm. D4: 50 mm. D5: 64 mm. In this experiment, substrate rotation: 0 rpm. PS sphere size in colloidal monolayer: 350 nm.
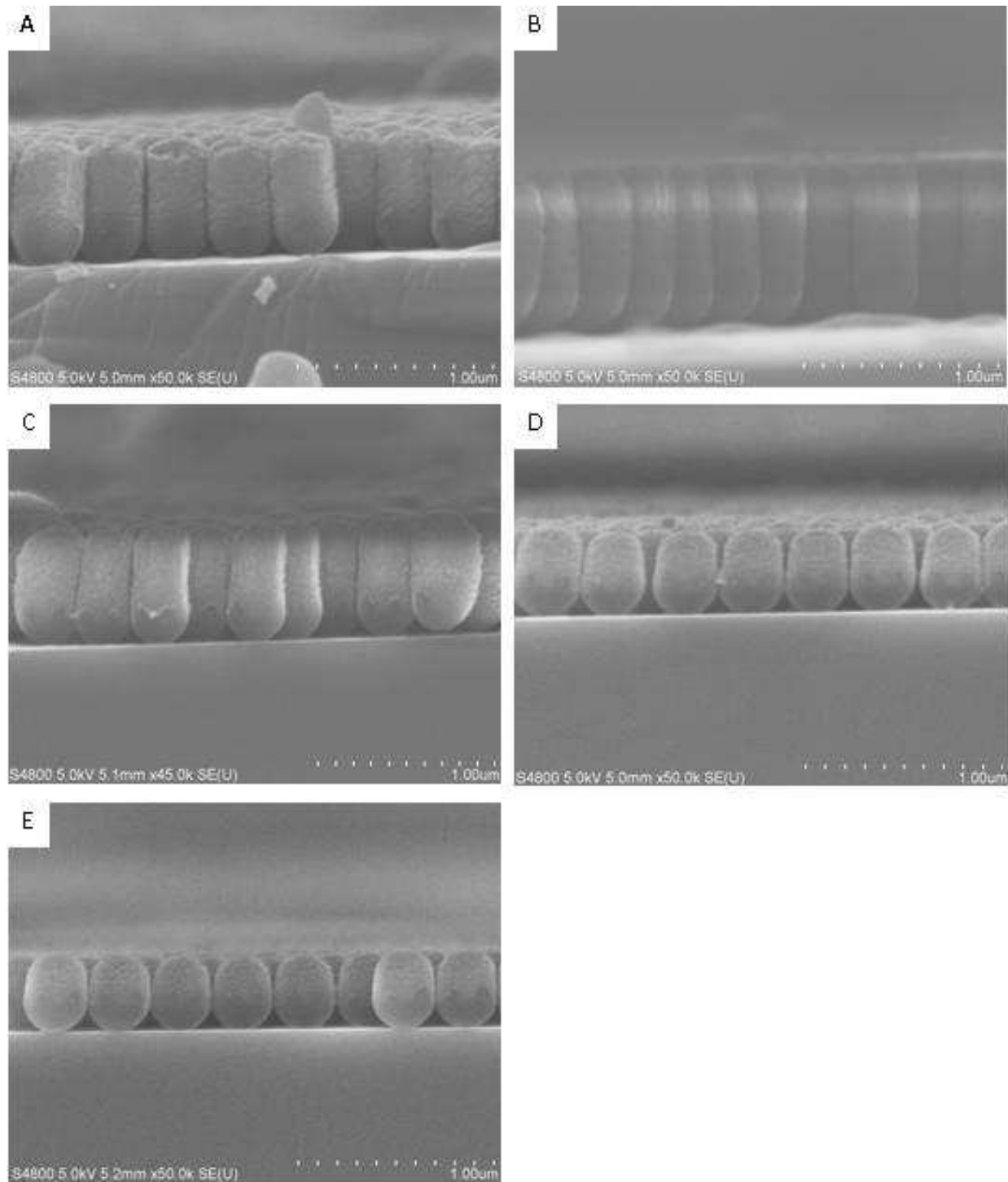
Fig. 14. FESEM cross-section images of the samples at different positions in Figure 10.
Images A to E are from the samples at positions D1 to D5.

2.3 Extension of PLD assisted colloidal lithography

The hexagonal close-packed (hcp) micro/nanostructured arrays can be obtained by PLD using colloidal monolayer template. Such PLD assisted colloidal lithography can be extended to prepare hexagonal non-close-packed (hncp) micro/nano- particle or nanorod arrays by further annealing process. [85-88]

PS colloidal monolayer was first fabricated on Si substrates by a self-assembly process. It was then placed in a PLD chamber for deposition at room temperature. After deposition, the sample was moved to an oven from the PLD chamber and annealed in air. The hncp, hierarchically ordered micro/nano- particle arrays were thus prepared on the substrate, as illustrated in Figure 15.[85]

Figure 16 shows FE-SEM images of the TiO_2 hierarchical hncp micro/nano- particle array obtained by PLD assisted colloidal lithography and subsequently annealed at 650 ℃ for 2 h in air. One can clearly find that this particle-ordered array takes on hncp arrangement. Each particle in the periodic array exhibits a hemispherical shape with an average size of 240 nm (Figure 16c) and is composed of small nanoparticles (Figure 16d). Additionally, SEAD pattern (inset in Figure 16d.) indicates the deposited materials are changed from amorphous to anatase typed TiO_2 after annealing. These results reflect that this hncp particle array possesses a hierarchical micro/nano-structure.

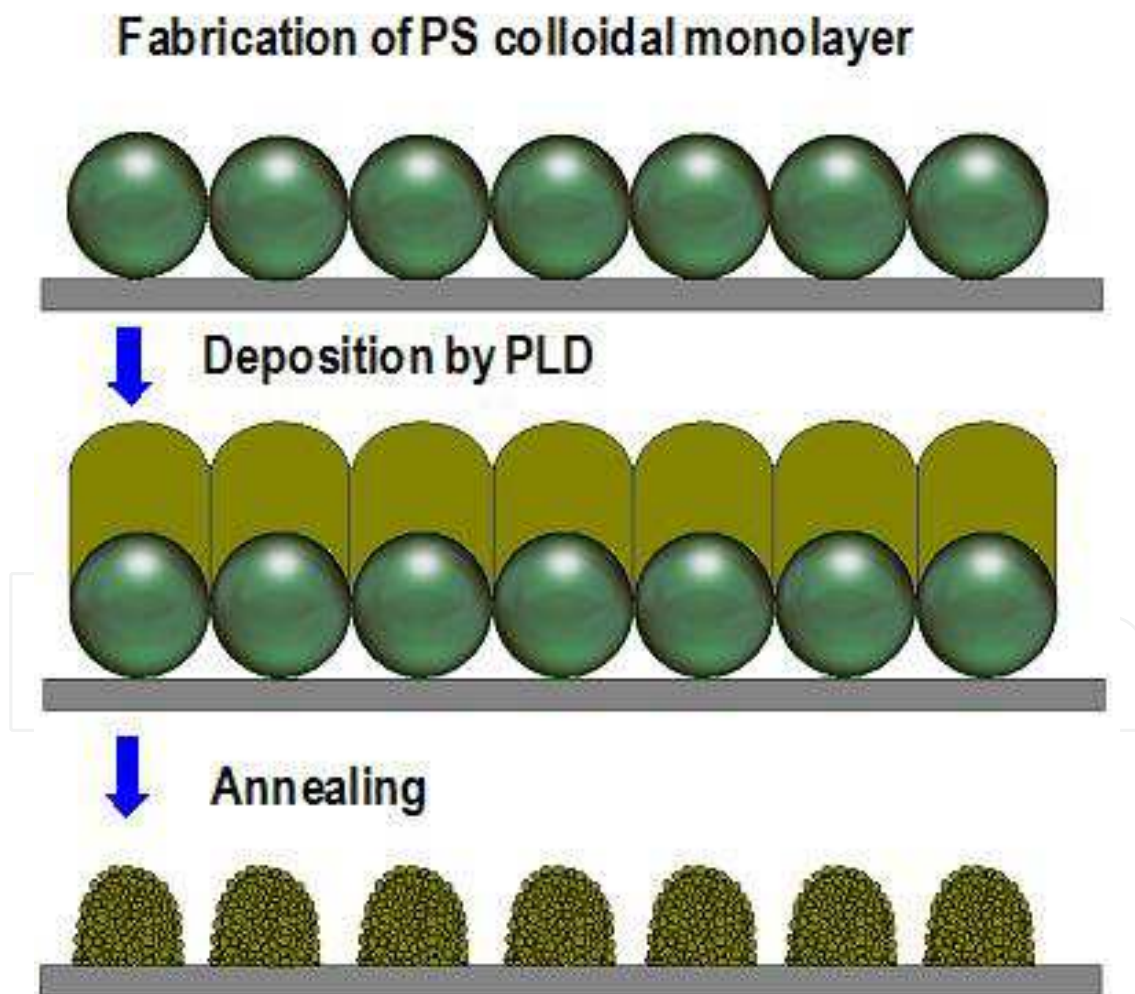

Fig. 15. Schematic illustration of fabrication process for the hierarchical hncp micro/nano-particle array.
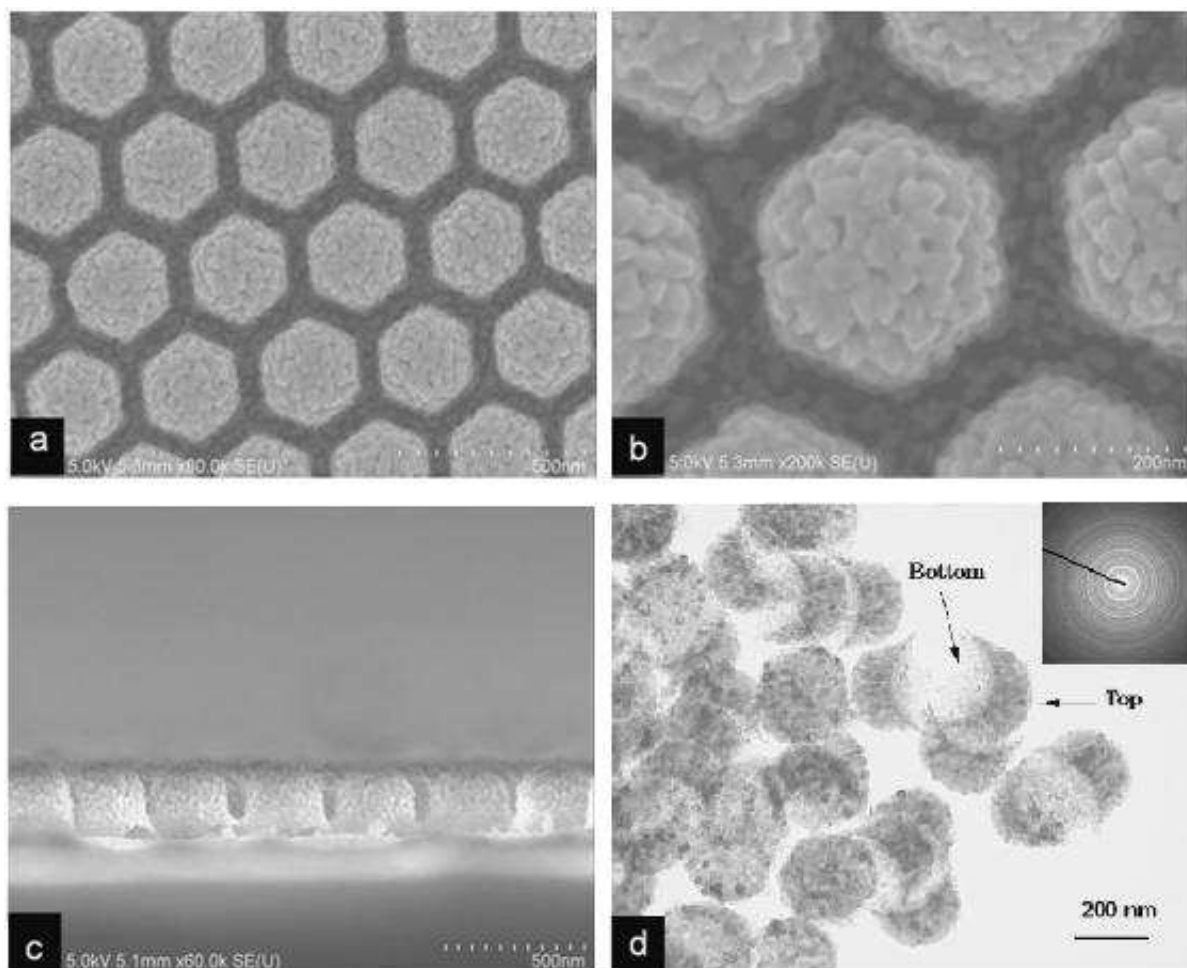
Fig. 16. FE-SEM and TEM images of the hierarchical hncp micro/nano particle arrays. a)-c): FE-SEM images. a) Large area hierarchical micro/nanostructured array b) Same at high magnification. c) Cross section d) TEM image of hierarchical particles (scratched from the supporting substrate by a knife and transferred to TEM copper grid for observation) and the corresponding SAED pattern (inset).

The formation of hncp, hierarchical micro/nano- particle array is discussed based on experimental results. Herein the explanation is given using TiO_2 as an example. The sample produced by PLD assisted colloidal lithography without further heating displayed an hcp alignment (Figure 17a). TiO_2 was deposited on the PS sphere surfaces and grew along the vertical direction (Figure 17b). Each particle is composed of two parts: the PS sphere at the bottom and an amorphous, porous TiO_2 layer consisting of smaller particles on the top (Figure 17c, d). The amorphous materials crystallize after being annealed at high temperature. In this case, when the amorphous TiO_2 with its supporting PS spheres was heated at 650 °C for 2 h, the PS spheres were burned out. Meanwhile, the TiO_2 particles on top of the PS sphere were changed to anatase polycrystals composed of smaller nanoparticles of ca.30 nm and were dropped vertically down to the original position of the PS sphere. Additionally, the volume of TiO_2 particles decreased during the change from the amorphous to the crystalline phase and hence an hncp hierarchical particle array was formed on the substrate, as illustrated in Figure 18. The hierarchical hncp mciro/nano-particle array film adhered tightly to the substrate after annealing and could not be detached from the supporting substrate even when it was washed ultrasonically in water for 30 min.
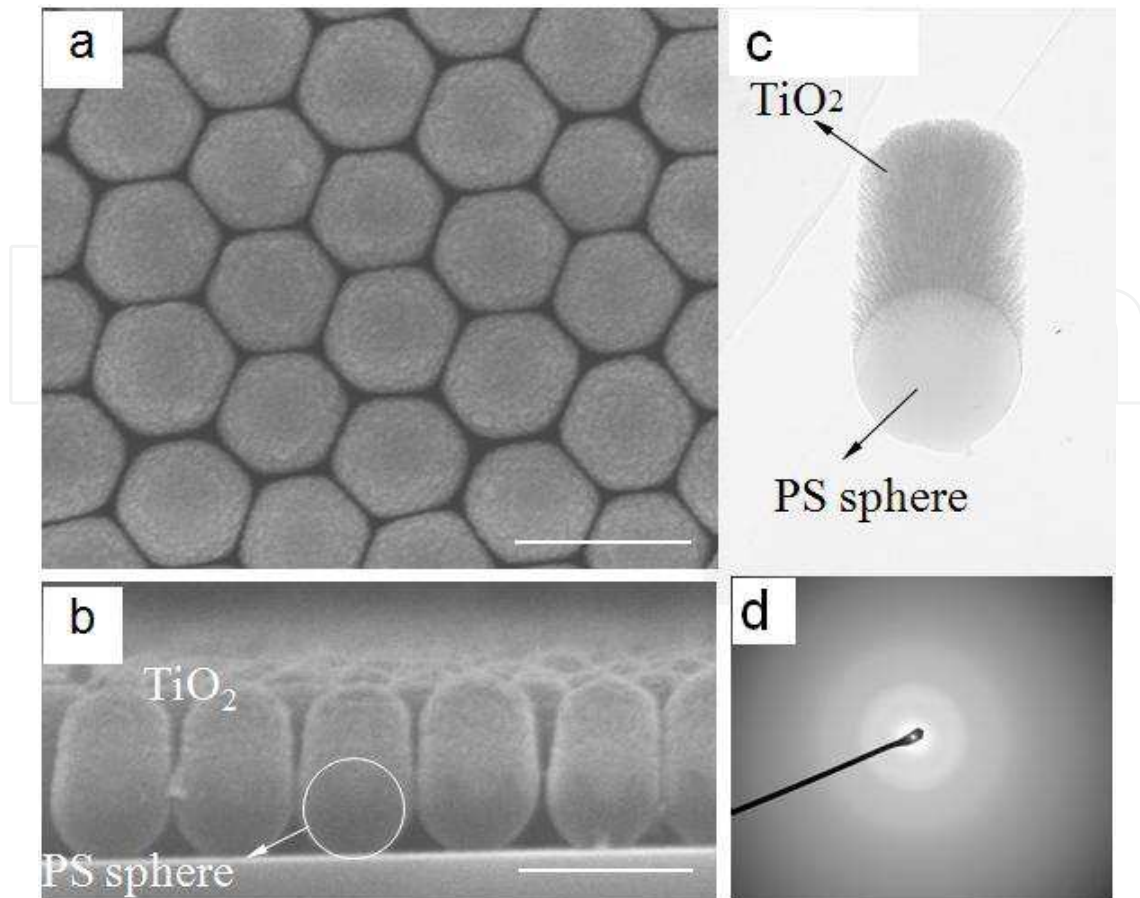
Fig. 17. (a, b): FE-SEM images of the as-deposited sample produced by the PLD in ambient atmosphere without heating. a) Top-view image. b) Cross-sectional image. c) TEM image of single unit. d) SAED pattern of deposited materials.
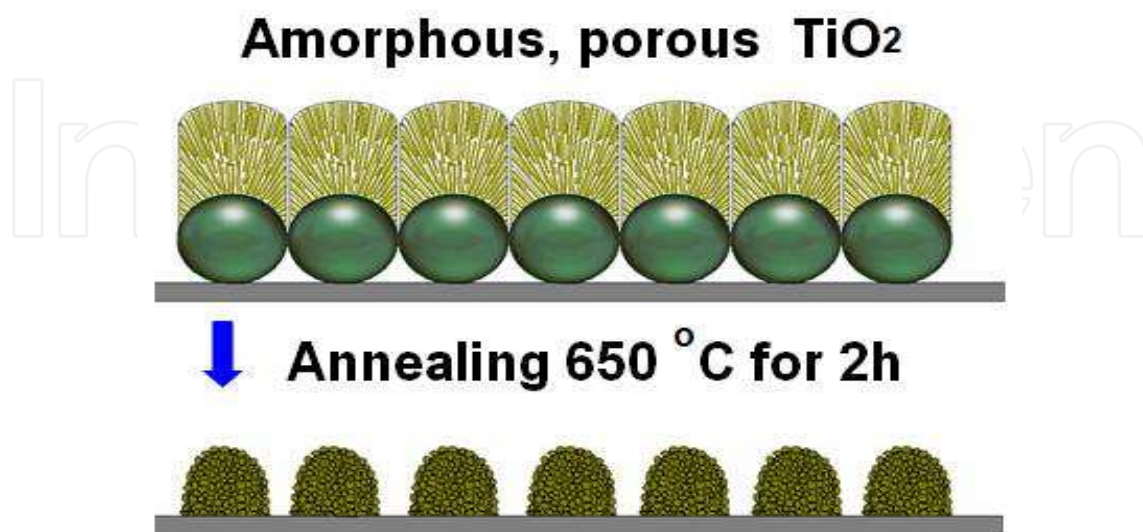
Fig. 18. Formation of hierarchical *hncp* micro/nanostructured particle arrays.
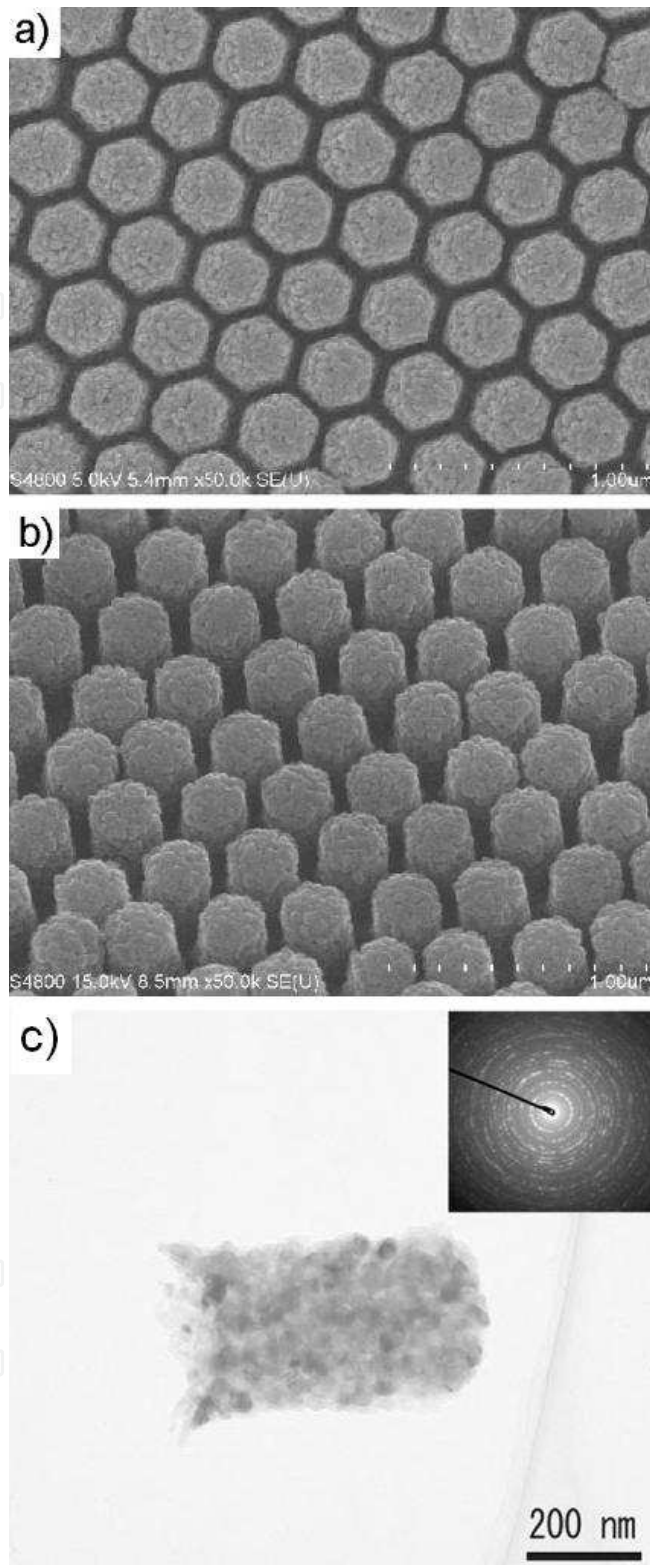
Fig. 19. (a, b) FE-SEM images of a nanorod array by PLD using a colloidal template monolayer with 350 nm PS spheres in O_2 at a pressure of 6.7 Pa for 60 min and subsequent annealing in air. a) A top-view FE-SEM image. (b) An FE-SEM image of a sample tilted to 45o. (c) TEM image of a nanorod and the corresponding selective area electron diffraction (SAED) pattern (inset).

In the PLD assisted colloidal lithography, if the deposition time increases to a appropriate time, an hncp micro/nano rod array can be obtained after PLD and subsequently annealing.[86] Figure 19 presents FE-SEM images of the hierarchical micro/nano rod array obtained by PLD assisted colloidal lithography (PS sphere size: 350 nm; background O_2 pressure: 6.7 Pa; longer deposition time: 60 min) after annealed at 650 ℃ for 2 h in air. Figure 19 a and b indicate that a periodic nanorod array takes an hncp arrangement and that each nanorod consists of many nanoparticles. The TEM image (Figure 19c) of a single nanorod shows that it has an aspect ratio of ca. 2:1 and is composed of small nanoparticles, and the PS sphere templates were entirely removed during annealing. The hncp micro/nano- rod arrays originated from amorphous, hcp micro/nanostructured array produced by PLD at room temperature without annealing, as displayed in Figure 20. Beside amorphous materials deposited by PLD, some crystalline materials, e.g. Fe_2O_3, their hncp micro/nanostructured arrays can be also achieved by PLD assisted colloidal lithography after annealing. Figure. 21a, b present SEM images of hierarchical, hcp, crystalline Fe_2O_3 micro/nanostructured arrays by PLD at oxygen pressures of 6 Pa at room temperature. Such sample was annealed in air at 450 ℃ for 3 h and, PS colloidal monolayer template was completely decomposed and hierarchical hncp micro/nano-structured array was formed, as shown in Figure 21 c-f.
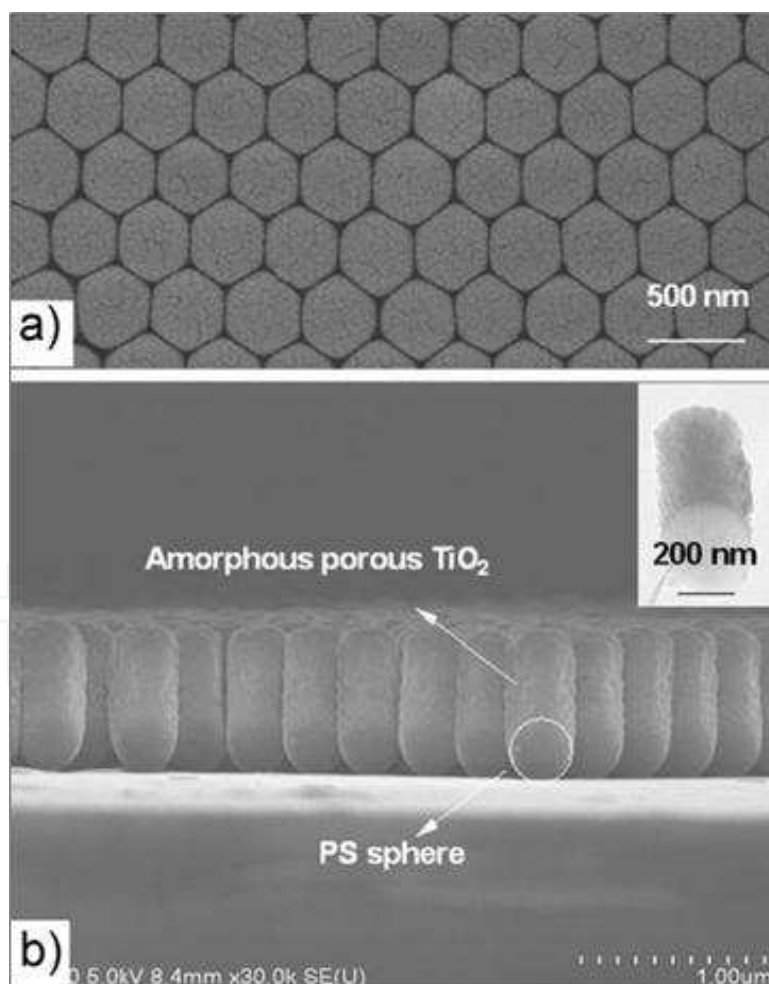
Fig. 20. FE-SEM images of an amorphous TiO_2 hcp nanorod array on the colloidal monolayer before annealing. a) Observation from top, b) Cross section. Inset in (b): a TEM image of a single amorphous TiO_2 nanorod with PS sphere.
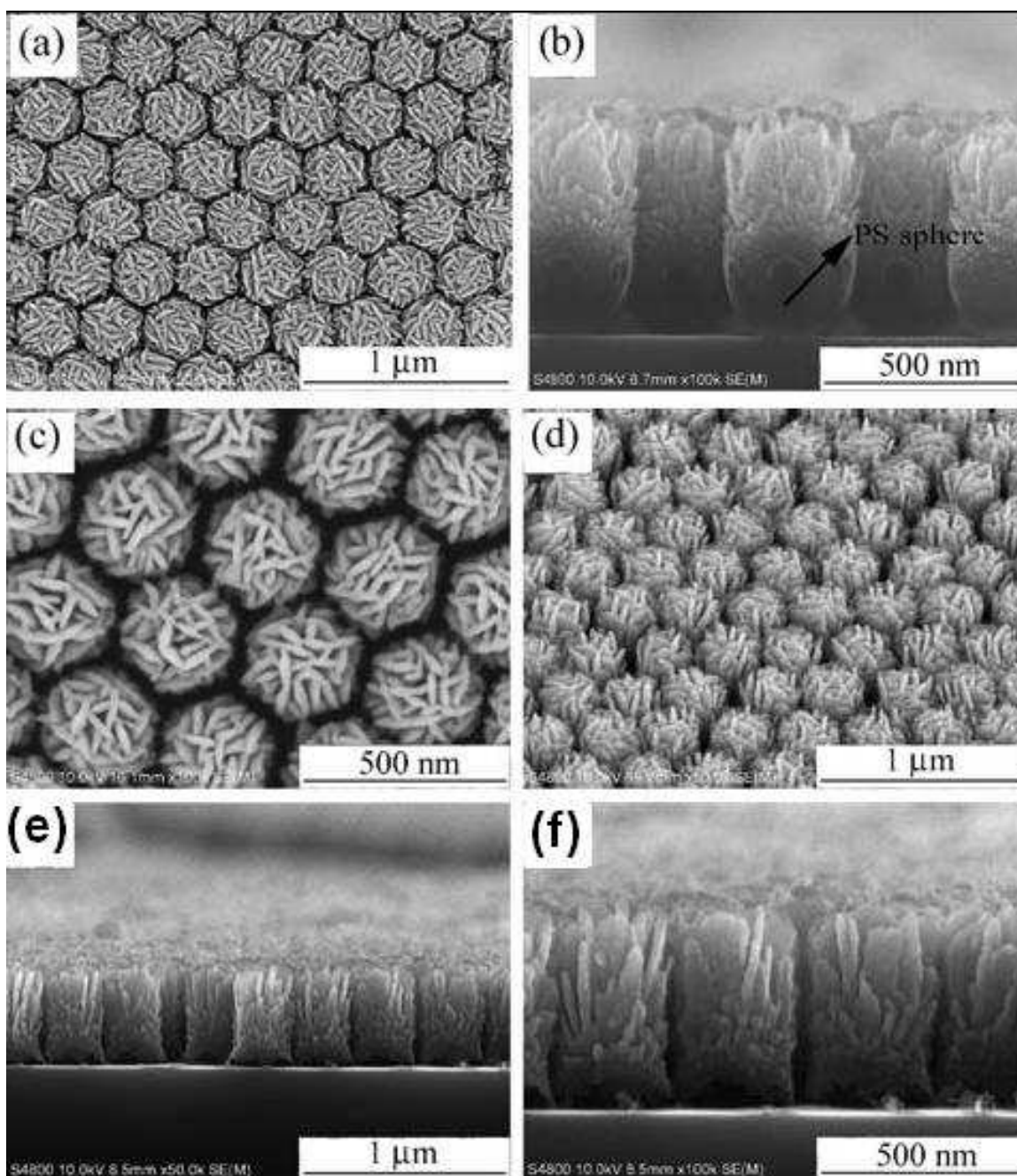
Fig. 21. SEM images of Fe$_2$O$_3$ micro/nanostructured array based on colloidal monolayer template and PLD at the oxygen pressure of 6 Pa. (a, b) Before (c-f) after annealing 450 °C for 3 h in air. (c) Top-surface image. (d) 45° tilted view. (e) Cross-section image. (f) Higher magnification.

In this route, the interspace between two neighboring rods can be controlled by changing the background gas pressures in PLD process. Usually, the porosity and specific surface area of the rods in arrays can be tuned by varying the background gas pressure in PLD deposition and they increase with increase of background gas pressure (Figure 22a–c). Therefore, the interspace between neighboring anatase rods can be tuned with different background gas pressures in an hncp array after annealing. The interspace will increase with increasing background gas pressure (Figure. 22a'–c' and a''–c'').
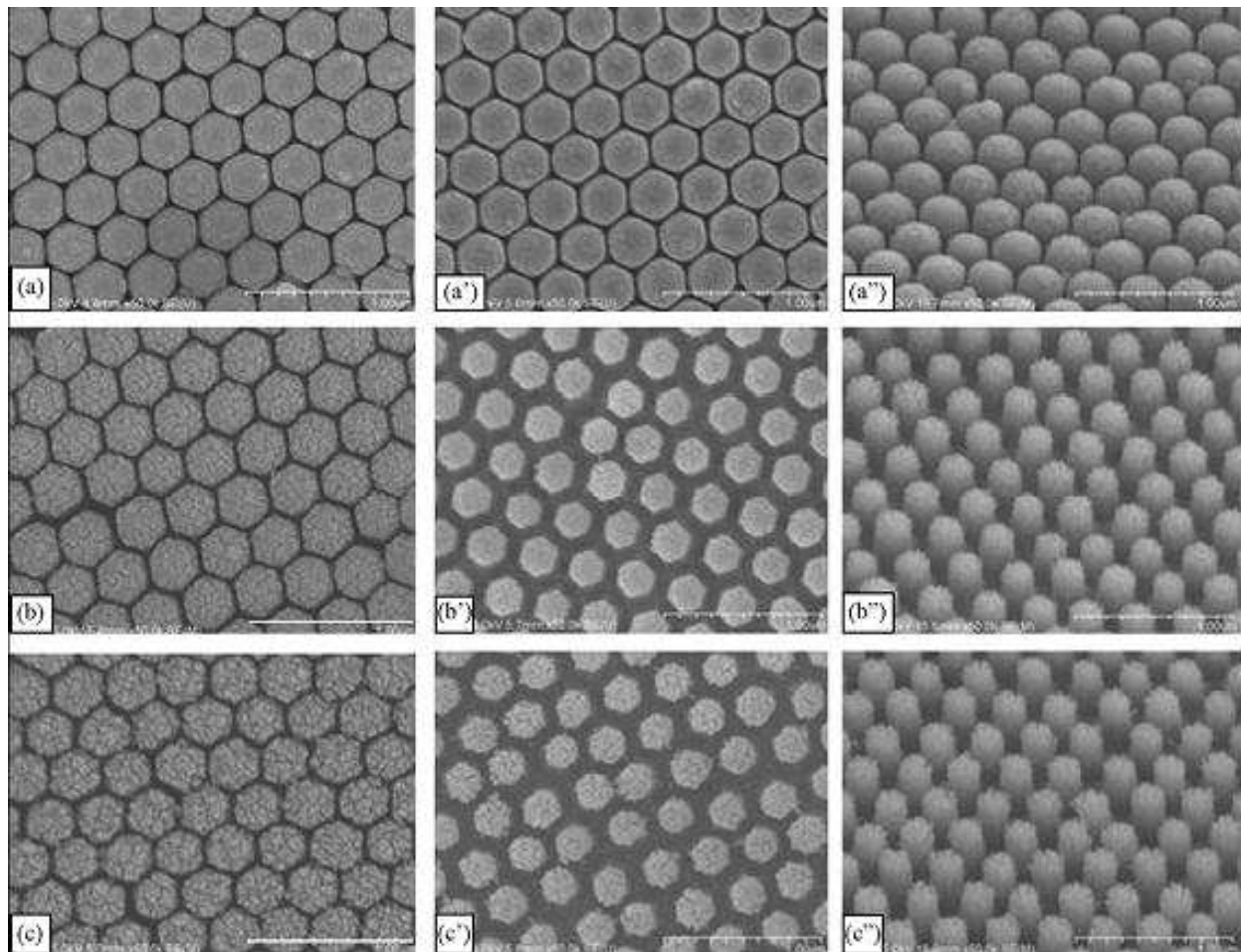
Fig. 22. FE-SEM images of an amorphous hcp TiO$_2$ nanorod array and anatase hncp TiO$_2$ nanorod arrays obtained by PLD under different background gas pressures and subsequent annealing. PLD was performed in oxygen (a) at 2.0 Pa for 200 min; (b) at 16.8 Pa for 43 min; (c) at 26.8 Pa for 30 min. (a–c) before annealing, (a′–c′) top views after annealing, (a″–c″) tilted view with 45 degrees after annealing.

3. Sputtering assisted colloidal lithography

In this method, a PS colloidal monolayer on a substrate is placed into the chamber of radio frequency (RF) magnetron sputtering for material deposition at room temperature and Ar is introduced as the background gas.[89] A unique hncp hierarchical micro/nanostructured array is formed due to PS-templated plasma etching/deposition in a relatively high vacuum (0.06 Pa). The features of this technique are (1) low-pressure sputtering; (2) PS-templated sputtering, which guarantees a periodic arrangement, and (3) plasma etching/deposition, which eventually produces the unique hncp hierarchical micro/nano-structure.

Figure 23 presents FE-SEM and TEM images of hierarchical alumina mciro/nanostructured arrays by sputtering target alumina using a PS colloidal template with a sphere size of 750 nm in a relatively high vacuum (0.06 Pa). They show the following three unique features. First, it is a periodic nanocolumn array cushioned by a semi-shell in an hncp arrangement. Each nanocolumn is composed of two parts: a semishell- shaped cushion at the bottom and a vertical nanocolumn on the top of the cushion. Such nanocolumn possesses a very rough

structure on the surface and seems to be composed of many minicolumns, indicating that the sample possesses a hierarchical, porous structure and hence has a high surface area. Secondly, the periodicity was 750 nm, matching well with the initial size of the PS spheres. It is very evident that the sizes of the cushion and the central columns were reduced by about 15% and 45% compared to the original size of the PS template.

The formation of such hierarchical micro/nanostructured arrays is traced by the different sputtering deposition time, as demonstrate in Figure 24. With increase of deposition time (Figure 24 A–D), the PS sphere size gradually decreases and the alumina columns grow vertically in the center, finally the columnar structures and a salver-shaped semi-shell are formed. Generally, thin alumina continuous film is formed on bare substrate without PS spheres due to the strong ion energy and subsequent rapid surface migration under such a low sputtering pressure. In the case with PS sphere array on the substrate, alumina components sputtered from the target are impinged and implanted into the PS due to the strong ion energy and soft nature of PS. The part of PS sphere is also continuously etched away by argon ions and part of deposited alumina is also etched away, but remaining part will gradually form a structure. Additionally, the PS colloidal monolayer supplies the periodic array template. Merging these two aspects into one forms a unique hierarchical micro/nano-structured arrays. The PS spheres become smaller with plasma etching and a salver-shaped semi-shell gradually appear. Further sputtering causes the PS spheres to be etched more significantly, and the species generated from the target deposit perpendicularly onto the template (both the center and the semi-shell part), thus forming a column structure and salver-shaped semi-shell. Implanted components of aluminium and oxygen into PS sphere will be linked together by continuous etching of PS. But at the side edge of the spheres, the amount of PS is not much and easily etched away to form aluminium oxide film, resulted in the cushion shell. The amount of PS at the center part is much more and even by continuous etching a film cannot be formed and rod-like structures are generated. Further sputtering continues etching the PS sphere until the final unique hncp hierarchical structure forms. The formation process of this unique hierarchical mciro/nano-structure is schematically illustrated in Figure 25. In order to further confirm this process, the pressures of Ar were adjusted from low level (0.06 Pa) to 0.13 and final 6.7 Pa. The FE-SEM images of the samples are presented in Figure 26. With increase of the background gas pressure from 0.06 Pa to 0.13 and 6.7 Pa, the collision probability between the ejected species and Ar molecules increases, thus the PS spheres are more significantly etched and no semi-shell can form. Therefore, only columnar structures are obtained (Figure 26). The amounts of deposited materials in the inter-columnar structures are negligible probably due to the blocking effects of gaseous species emitted from decomposed PS spheres during sputtering. These results firmly prove that a relatively high vacuum condition subsequently induces mild plasma etching/deposition. Besides hncp alumina micro/nano-structured arrays with a periodicity of 750 nm, novel hierarchical arrays with periodicities of 350 nm, 1 μm, and 2 μm were also created by colloidal monolayers with different PS sphere sizes during sputtering at the same pressure of Ar as in Figure 27. Besides alumina, hierarchical arrays of other materials including Au/Al_2O_3 composite, CuO, and NiO can also be fabricated by the presented one-step plasma etching. Some of the results are presented in Figure 28. In this method, only the inorganic materials can be used as the deposited materials. Otherwise, the deposition cannot be guaranteed because of the subsequent etching.
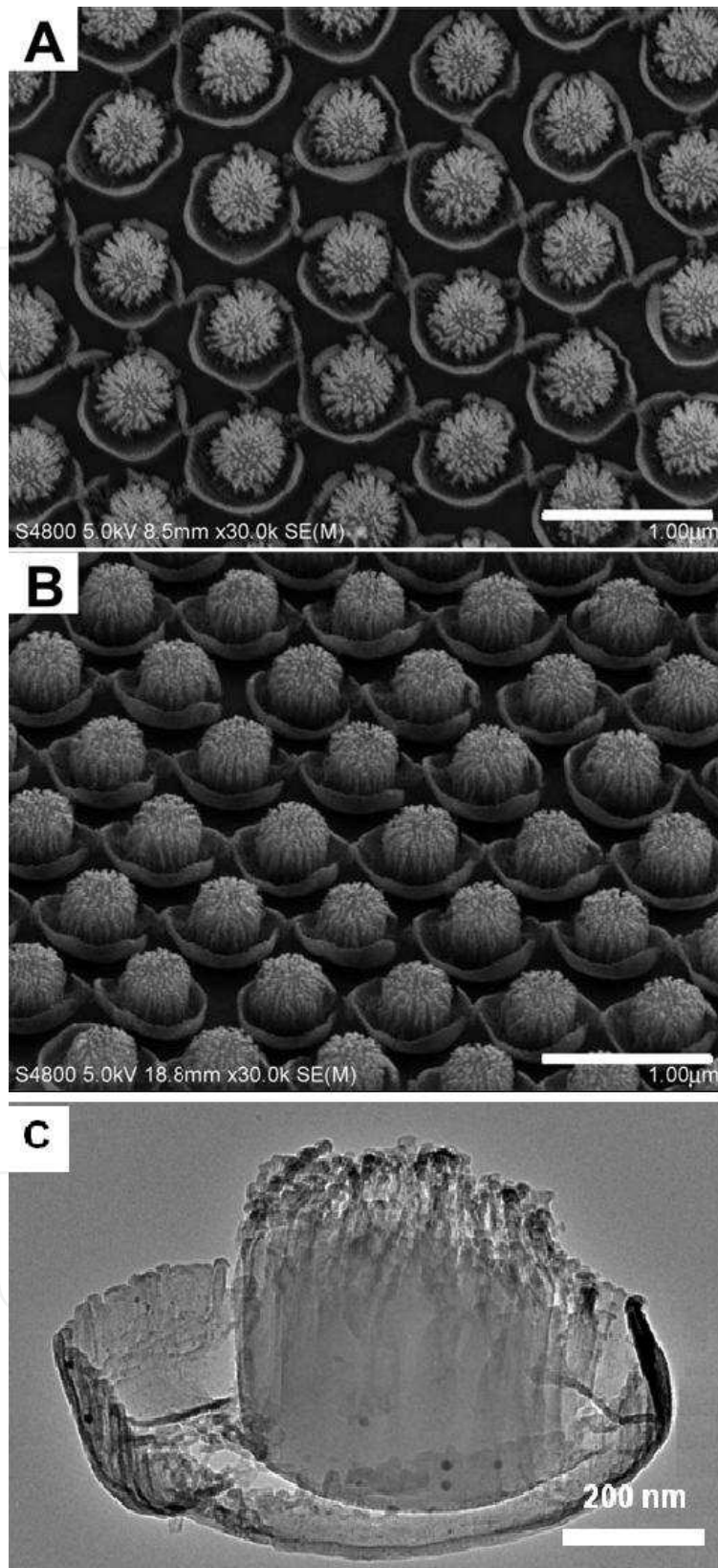
Fig. 23. FE-SEM (A, B) and TEM (C) images of a sample obtained by sputtering using a PS colloidal monolayer as the substrate (PS sphere size: 750 nm; deposition time: 2 h). (A) Top view. (B) Titled view with 45° angle. The scale bar in A, B: 1 μm. (C) TEM image of one unit.
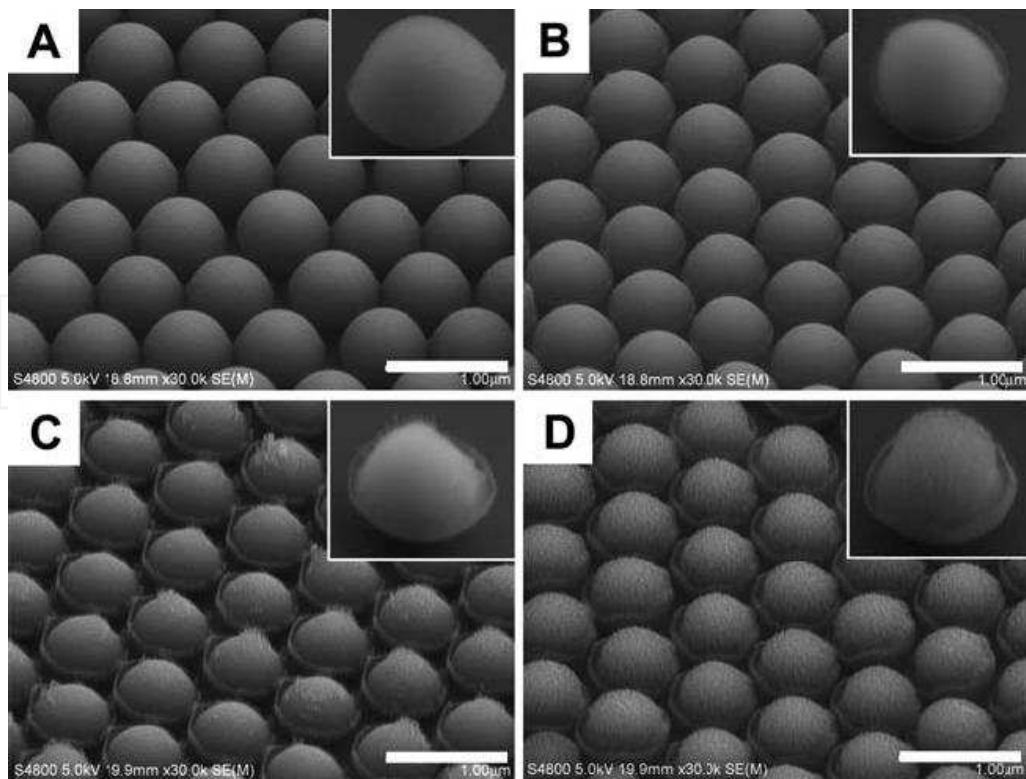
Fig. 24. FE-SEM images of samples obtained with different deposition times. (A) 10 min. (B) 25 min. (C) 30 min. (D) 60 min. The inset is high-magnification image of one unit in each figure.
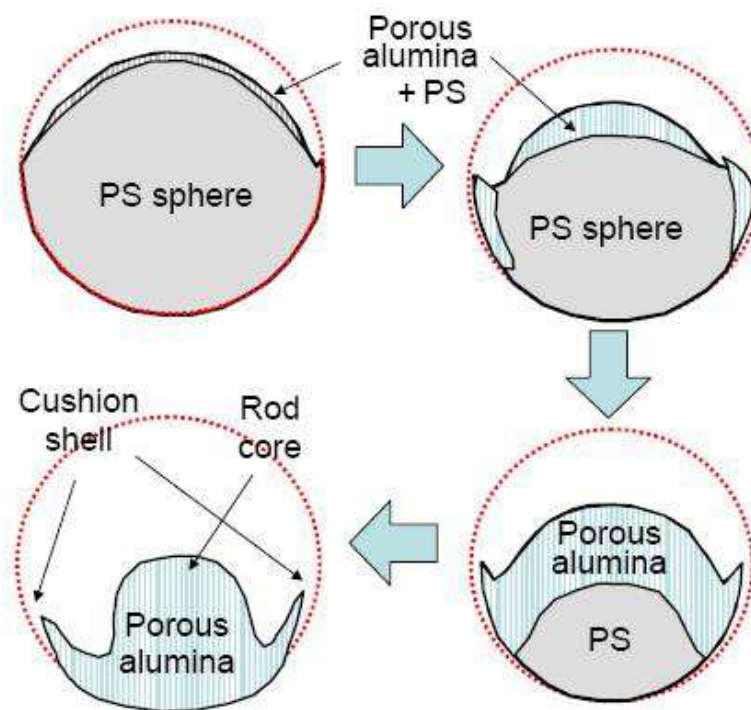
Fig. 25. Schematic illustration of the formation process of unique hncp hierarchical micro/nano-structure.
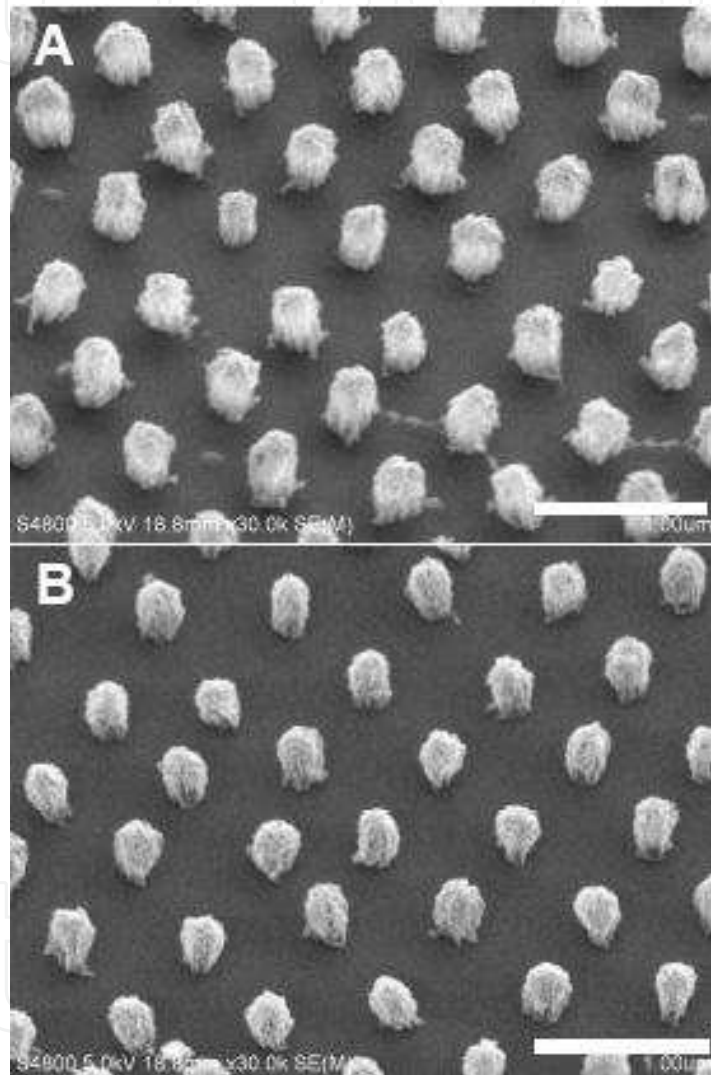
Fig. 26. FESEM images of a sample obtained by sputtering using a PS colloidal monolayer as the substrate at Ar pressures of (A) 0.13 Pa and (B) 6.7 Pa (PS sphere size 750 nm; deposition time 2 h). These images are observed with a tilt angle of 45°. The scale bar is 1 μm.
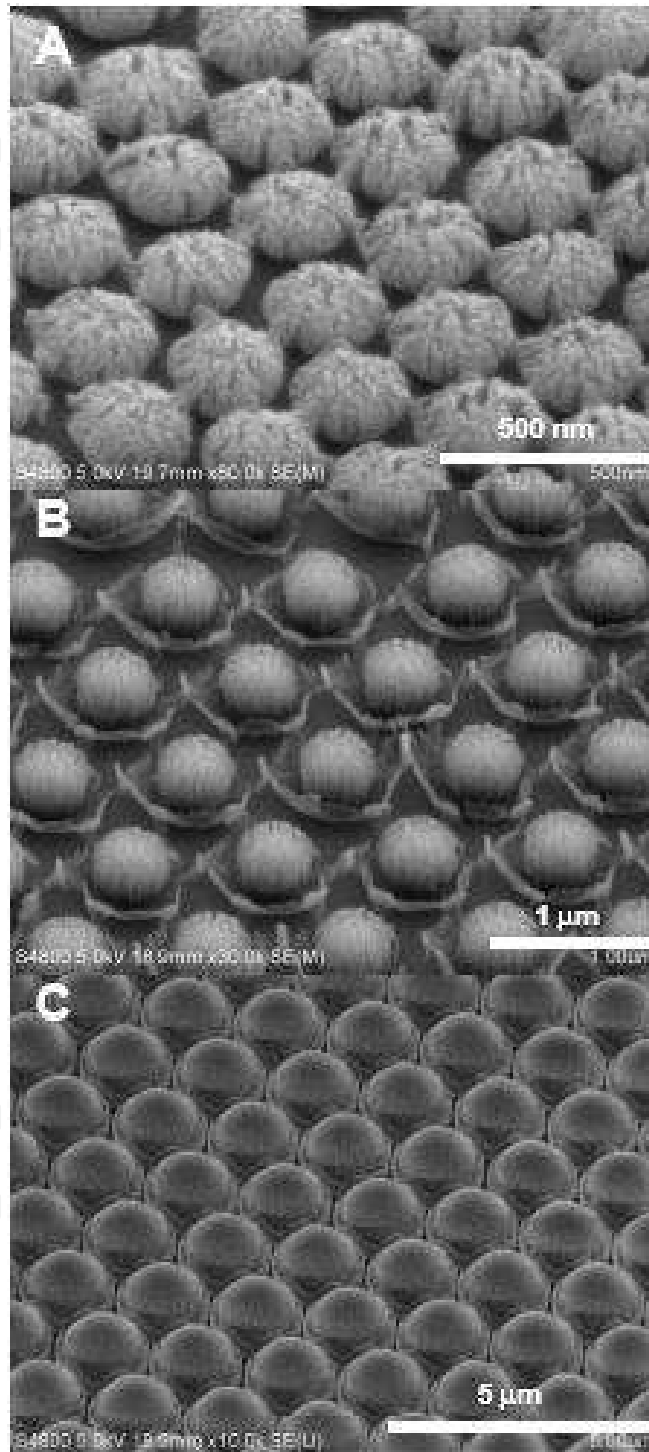
Fig. 27. FESEM images of a sample obtained by sputtering using a PS colloidal monolayer template with different PS sphere sizes at 0.06 Pa. (A) 350 nm. (B) 1 μm. (C) 2 μm.
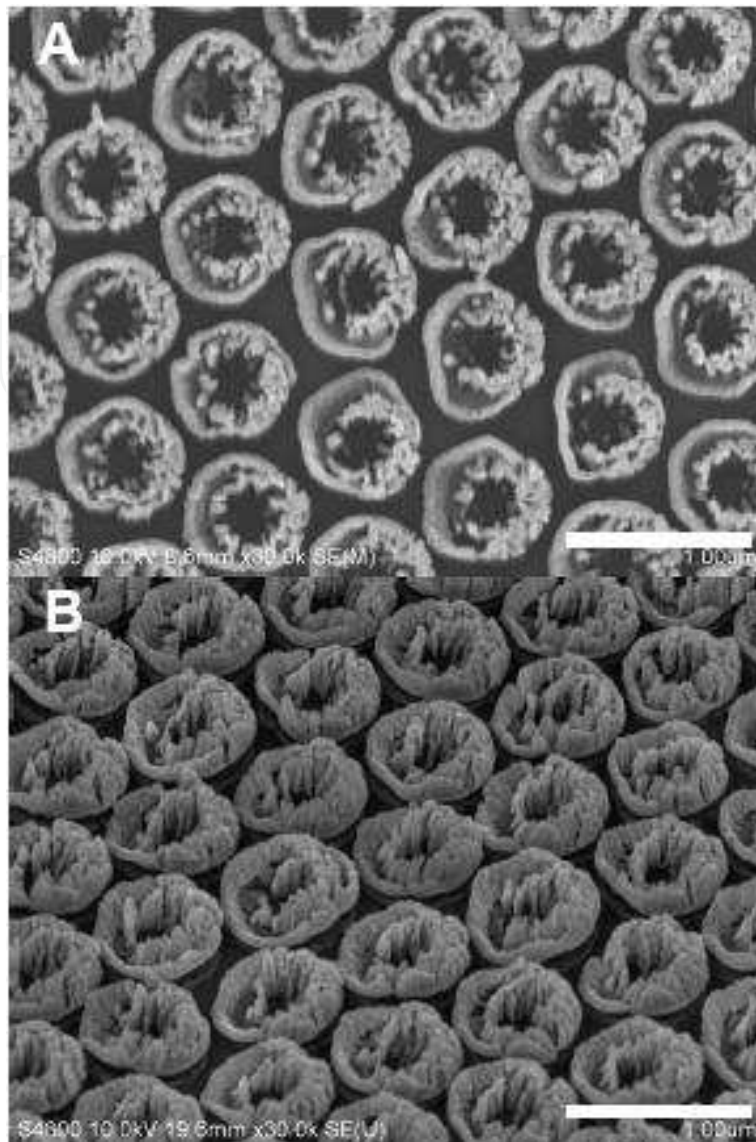
Fig. 28. FESEM images of periodic Au/Al$_2$O$_3$ nanocomposite arrays obtained by co-sputtering multiple targets consisting of an Al$_2$O$_3$ target and Au sheets and using a PS colloidal monolayer as the substrate (PS sphere size 750 nm; deposition time 2 h). (A) Image observed from the top. (B) Image with a tilt angle of 45°. The scale bar is 1 μm.

4. Applications of periodic micro/nanostructured arrays

Based on colloidal monolayer templates, the different hierarchical micro/nanostructured arrays can be fabricated by physical deposition and their morphologies and structural parameters (sizes and interspace of micro/nanostructured unit) can be facilely controlled by periodicities of colloidal monolayers, experimental conditions such as deposition time, background gas pressure etc. Some properties, such as the surface wettability, field emission, catalytic properties are closely morphology and structural parameter-dependent. These properties can be readily optimized by changing morphologies and parameters of the periodic arrays. Their investigations supply useful theoretic foundations and are highly valuable for designing micro/nanodevices based on these special arrays.

4.1 Wettability

Wettability is generally related to the surface morphologies, roughness and free energy of materials surface and it is evaluated by the water or oil contact angle. A special surface with self-cleaning effect is usually defined as a surface that has the ability to remove dirt or contaminants that are on it when water droplets slide along the surface. Self-cleaning is closely related to surface wettability[90-94]. The self-cleaning effect is normally attributed to superhydrophobicity (water contact angle (CA) exceeding 150° and sliding angle (SA) less than 10°) or superhydrophilicity (water CA less than 10°) of the surface. For superhydrophobicity with a self-cleaning effect, contaminants adhere to the water droplet surface and are removed after the water droplet slides off the solid surface with a small tilted angle, due to large water CA and low surface free energy. For superhydrophilic surfaces, contaminants can easily be swept away by adding water droplets on them, due to very low water CA. Wettability can be enhanced by increasing surface roughness, according to Wenzel's equation: [95]

$$\cos \theta_r = r \cos\theta \tag{1}$$

where r is the roughness factor, defined as the ratio of total surface area to projected area on the horizontal plane; θ_r is the CA of film with a rough surface; and θ is the CA of film with a smooth surface. Obviously, increased roughness can enhance the hydrophobicity and/or hydrophilicity of hydrophobic and/or hydrophilic surfaces. The hierarchical micro/nanostructured arrays based on colloidal monolayers are actually rough films at the micro/nano-scale level. It is expected that such hierarchical micro/nanostructured arrays could induce surface superhydrophilicity or superhydrophobicity with a self-cleaning effect, due to their high roughness. Amorphous, porous hierarchical TiO_2 micro/nanostructured arrays were prepared by PLD assisted colloidal lithography (Figure 3)[73]. These arrays exhibited strong superhydrophilicity. When a small water droplet was dropped on a hierarchical structured array, the droplet spread out rapidly on the surface and displayed a water CA of 0° in a 0.225 s (Figure 29). Additionally, this hierarchical array film exhibited superoleophilicity when a small oil droplet was placed on the nanorod surface and the oil CA became 0° in 0.5 s (Figure 30). These results suggest that this amorphous hierarchical micro/nano-structured array had superamphiphilicity with 0° of both water CA and oil CA.

A TiO_2 film with superamphiphilicity can generally be obtained by UV irradiation, due to hydroxyl ions generated by oxygen defects or dangling bonds on its surface, induced by photochemical processes[96]. However, the TiO_2 hierarchical micro/nano- structured array film possessed superamphiphilicity without further UV irradiation. The ions (e.g., Ti^{4+}, and O^{2-}) and electrons are released into the PLD chamber and some oxygen species are lost in the vacuum environment in PLD after a TiO_2 target absorbs energy from laser irradiation by exceeding its threshold. Oxygen vacancies are produced in the deposited TiO_2 during PLD, converting relevant Ti^{4+} sites to Ti^{3+} sites that are favorable for dissociative water adsorption. Therefore, these defect sites microscopically form hydrophilic domains on the TiO_2 surface. However, the other parts surrounding the hydrophilic domain remain oleophilic on the surface. A composite TiO_2 surface having hydrophilic and oleophilic domains on a microscopically distinguishable scale demonstrates macroscopic amphiphilicity on the TiO_2 surface[96]. Additionally, a TiO_2 nanoparticle film prepared by PLD without a PS colloidal monolayer exhibited a water CA of 15° and an oil CA of 27° (Figure 31). The roughness of the hcp TiO_2 hierarchical micro/nano-structured array film

was greatly increased compared with that of the nanoparticle TiO$_2$ film produced by PLD without using a colloidal monolayer. According to Wenzel's equation, wettability is enhanced from amphiphilicity to superamphiphilicity. Therefore, the superamphiphilicity of the amorphous micro/nano-structured array originates from the combination of the amphiphilicity produced by PLD and the special rough structures of hcp hierarchical arrays.
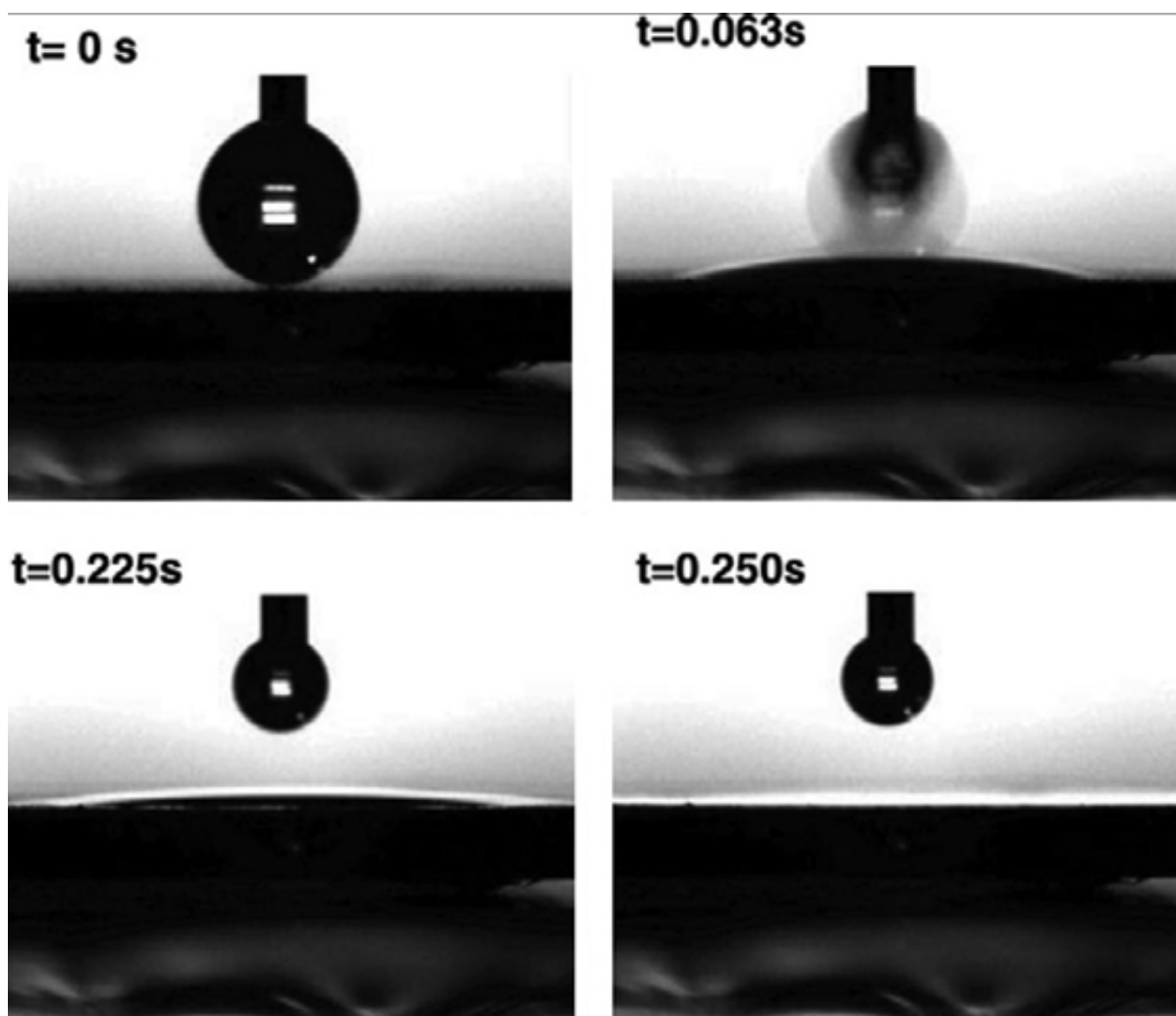

Fig. 29. Time course of water-contacting behavior on the amorphous TiO2 micro/nano-structured array film.
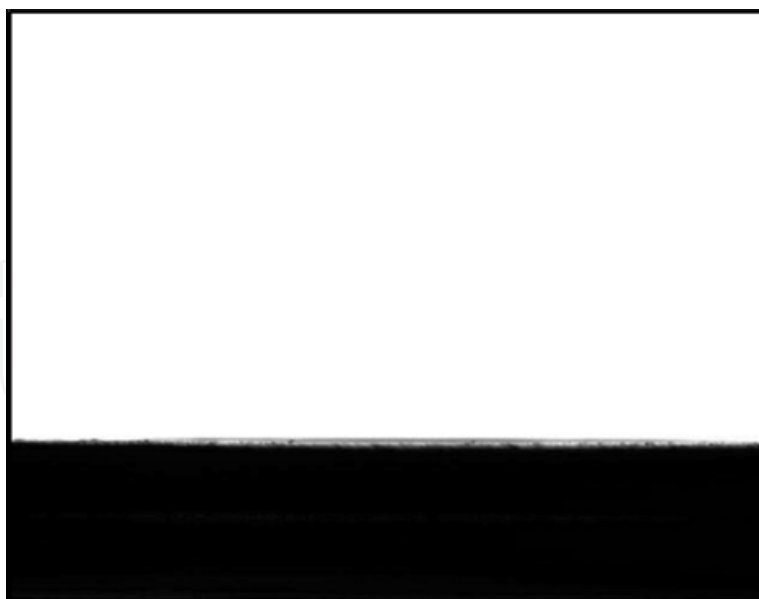
Fig. 30. Oil (rapeseed) droplet shape on amorphous TiO_2 micro/nano- structured array film. The oil contact angle becomes 0° in 0.5 s after it was dropped onto the surface.

More importantly, this amorphous TiO_2 hierarchical array demonstrated very good photocatalytic activity for organic molecular degradation (e.g., effective decomposition of stearic acid under UV illumination). A combination of superamphiphilicity and photocatalytic activity can yield a self-cleaning surface. For instance, an oily liquid contaminant spreads out on a surface due to superoleophilicity, which is helpful in improving the photocatalytic efficiency under light illumination. An organic contaminant including oil gradually degrades under sunlight irradiation (sunlight contains some UV light). The self-cleaning effect can be realized after washing away contamination from the superhydrophilic surface.

Additionally, superhydrophobic surfaces with large water CA and small SA have a self-cleaning effect. For superhydrophobic film, the surface should be sufficiently rough and have a chemical coating with low free-energy materials in order to trap the air on the rough surface. In this case, the area fraction of a water droplet in contact with the sample surface is very small, which helps obtain a small SA. Hierarchical periodic micro/nanostructured arrays based on colloidal templates provide surfaces with regularly ordered and well-defined roughness. They may lead to enhancement from hydrophobicity to superhydrophobicity on the surface after modification with low free-energy materials[97-99]. For instance, Co_3O_4 hierarchical, hncp micro/nano- rod arrays was created by PLD assisted colloidal lithography after annealing at 450 °C for 3 h (oxygen pressures: 93.1 Pa), as shown in Figure 32 a and b.[88] Such surface was chemical modification with fluorosilane, a kind of low free energy material, it presented superhydrophobicity with water CA of 152.6° and a very small SA, indicating self-cleaning effect. It can be explained by Cassie and Baxter equation,[100]

$$\cos\theta_r = f_1 \cos\theta - f_2 \tag{2}$$

Here, f_1 and f_2 are the surface area fractions of the projecting solid and air ($f_1 + f_2 = 1$). The large fraction of air trapped in the nanorod arrays forms a cushion at the film–water interface that prevents the penetration of water droplets into the grooves. In this case, θ_r is

152.6° and θ is 18.8°, so a value for f_1 of 0.06 is calculated from eqn (2) (i.e. f_2 is 0.94), implying that only 6% of the observed contact area beneath a water droplet is in contact with the water droplet. High f_2 of 0.94 means that the air was well trapped into the groove among nanorod arrays and hence the water droplet kept a spherical shape.
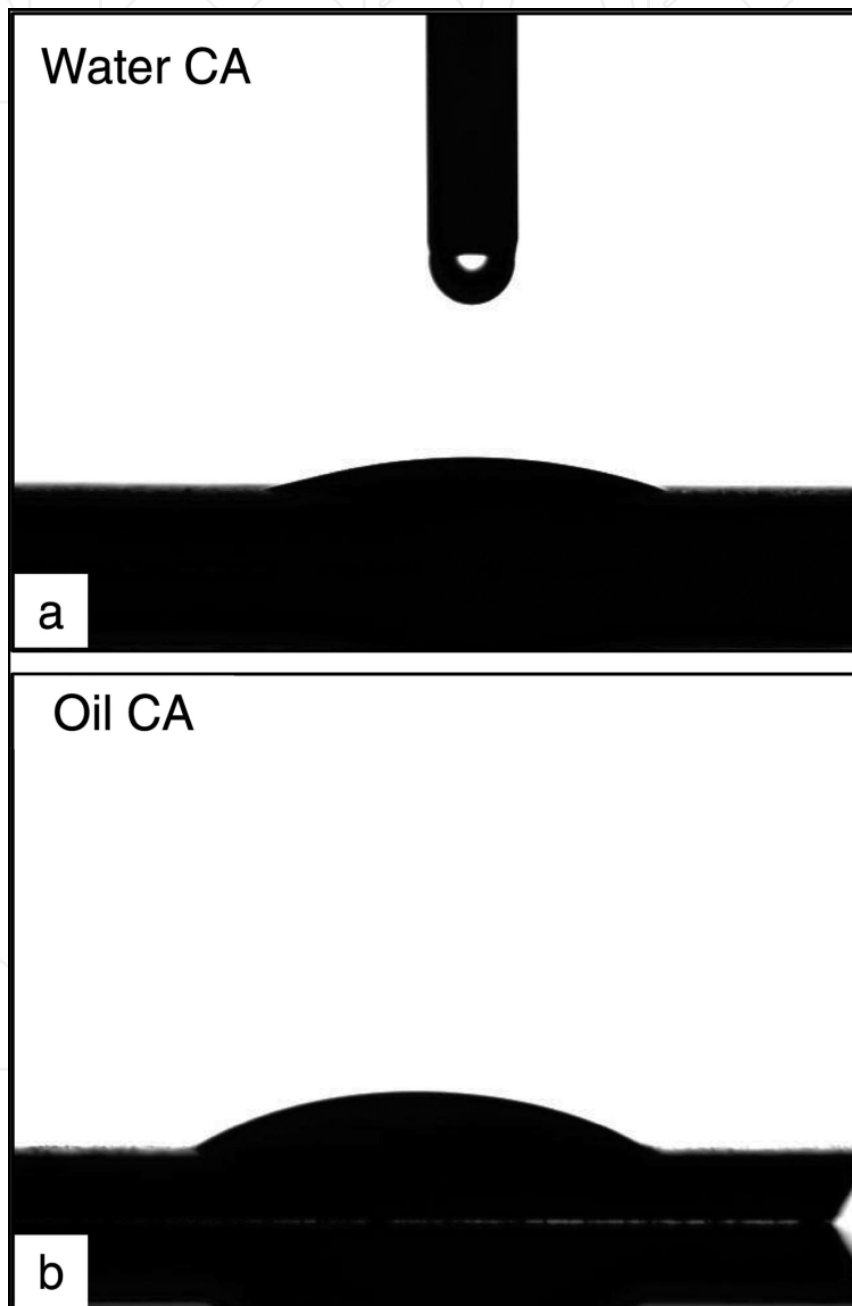
Fig. 31. Water and oil CAs on a TiO$_2$ film on a silicon wafer prepared by PLD without using a PS colloidal monolayer. (a) Water CA: 15 degrees. (b) Oil (rapeseed) CA: 27 degrees.
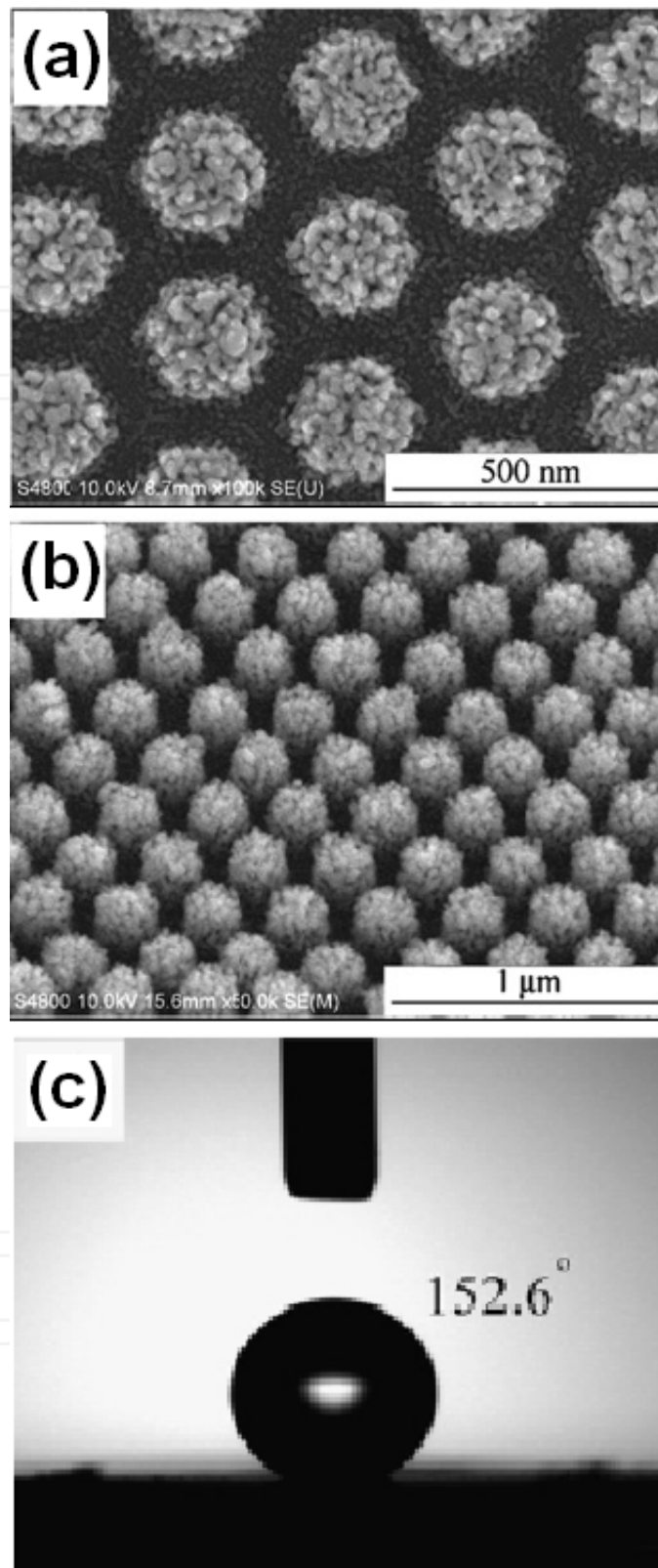
Fig. 32. FE-SEM images of Co$_3$O$_4$ hierarchical micro/nano- rod arrays obtained by PLD assisted colloidal lithography after annealing at 450 °C for 3 h (oxygen pressures: 93.1 Pa). (a) Top views; (b) Tilted at 45° (c) water CA after modification with low free energy materials.

4.2 Field emission

Field-emission (FE) properties have recently attracted so much attention due to great commercial interest in flat-panel displays and other microelectronic devices.[101] Besides carbon nanotubes, semiconductors have also attracted great interest in field emitters owing to their good mechanical stability, low work function, and high electrical and thermal conductivities.[102] FE properties are usually decided by the nature of the cathode materials as well as geometry and size of them. By well designing the geometry and size of cathode, for example, to introduce nanostructures on it, good FE performances have been achieved including faster turn-on time, compactness, and sustainability during the field emission compared to conventional bulky material forms. More importantly, researchers have found that cathodes composed of periodic regular arrays on the surface are very highly helpful for producing a low operating voltage and a stable current because of the elimination of the shield effect on densely packed 1D nanostructured arrays in field emission.

Periodic TiO_2 micro/nano-rod arrays with hncp arrangement can be synthesized by combining a colloidal monolayer template with pulsed laser deposition (PLD) followed by annealing in ambient air, as described before.[86] By this route, the periodicity of such special nanorods can be easily tuned by changing the colloidal sphere size in the colloidal monolayer template. While a distance between neighboring nanorods can be controlled by varying the background gas pressure during the PLD process if periodicity is fixed for a nanorod array. The well tunable periodicity and distance between neighboring nanorods are very useful for investigating and optimizing their FE performance.[86]

The periodic hncp TiO_2 nanorod array was fabricated by PLD using a colloidal monolayer template with 350nm PS spheres at 6.7 Pa O_2 for 60 min and subsequent annealing at 650 ºC for 2 h in air (Figure 19). It demonstrated a low turn-on field of about 5.6 V μm^{-1} (here the turn-on field was defined as the value of electric field when an emission current density was 4.5 nA cm^{-2}) according to the FE current density–applied electric field curve (J–E) at a working distance of 60 μm from the anode to the nanorod array serving as the cathode (Figure 33). This FE current–voltage characteristics can be expressed by a simplified Fowler–Nordheim (FN) equation and a field-enhancement factor, β can be defined as $B\phi^{3/2}/\kappa$ according to the FN equation (here ϕ: the work function of cathode material; κ: slope in FN plot).[103] This hncp TiO_2 nanorod array showed a field-enhancement factor β of 8.38×10^2. However, a TiO_2 nanorod array with top aggregation for several neighboring nanorods caused by longer deposition displayed a much higher turn-on field of 15.8 V μm^{-1} and lower field-enhancement factor b 3.34×10^2 (Figure 34). This result indicates that the good FE properties of a periodic TiO_2 hncp nanorod array are mainly attributable to the aligned and periodic hncp nanorod morphology.

When a periodicity of hncp nanorod array increased from 350 nm to 750nm and 1 μm by choosing the colloidal monolayers with different PS sphere sizes during the PLD at the same background gas pressure as before and followed by the same annealing, as presented in Figure 35. The field-enhancement factor decreased with increasing periodicity of the hncp nanorod array (Figure 36a). This is mainly attributed to a decreasing number density of nanorods with an increase in the hncp array periodicity. When the periodicity of the hncp nanorod array was increased from 350 to 750 nm, the turn-on field also increased from 5.6 to 13.0 Vμm^{-1}. When a periodicity further increased to 1 μm, the turn-on field remained about 13.0 Vμm^{-1}. It is evident that the hncp nanorod array with the smallest periodicity of 350nm exhibited the best FE properties in this investigation.
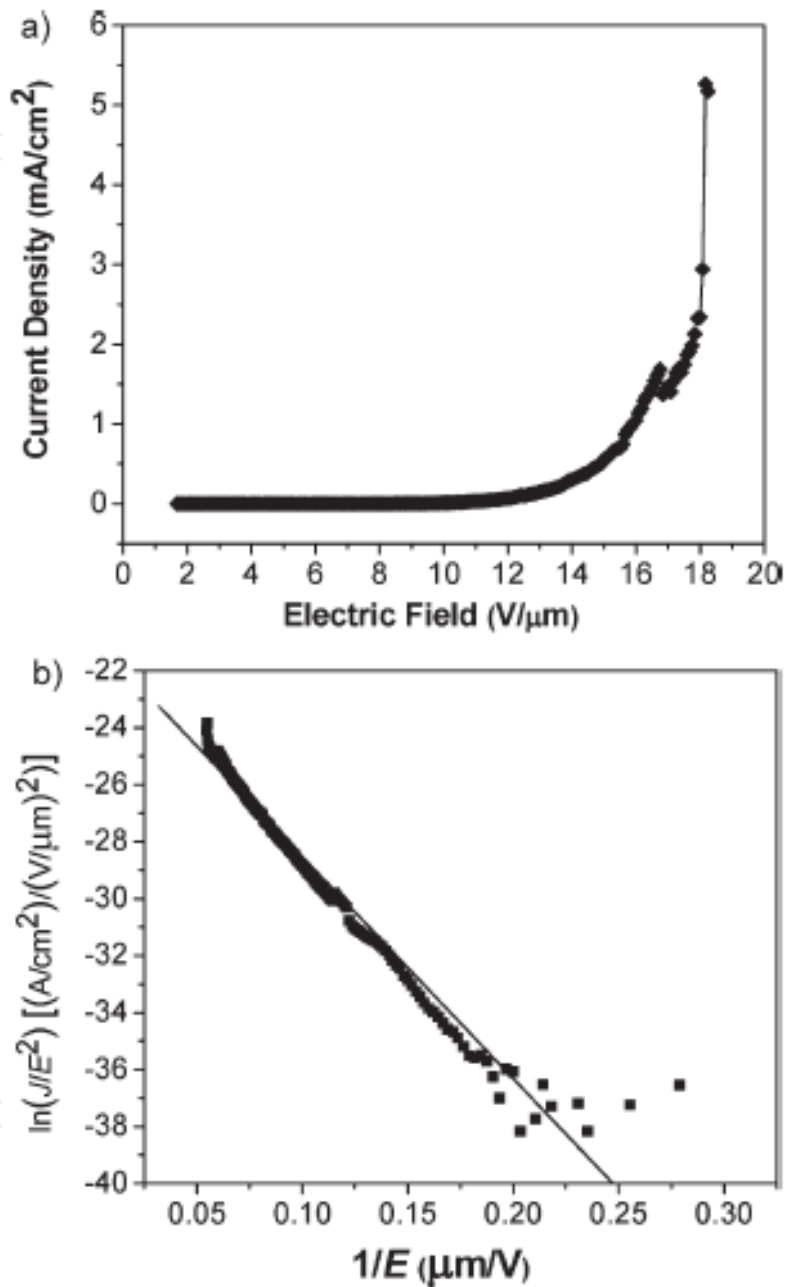
Fig. 33. FE properties of periodic hncp nanorod array by PLD using a colloidal monolayer template with 350nm PS spheres in O_2 at a pressure of 6.7 Pa for 60 min and subsequent annealing in air. a) FE current density–electric field (J–E) curves measured for an hncp TiO_2 nanorod array at an anode–cathode distance of 60 μm. b) Corresponding Fowler–Nordheim (FN) plot.
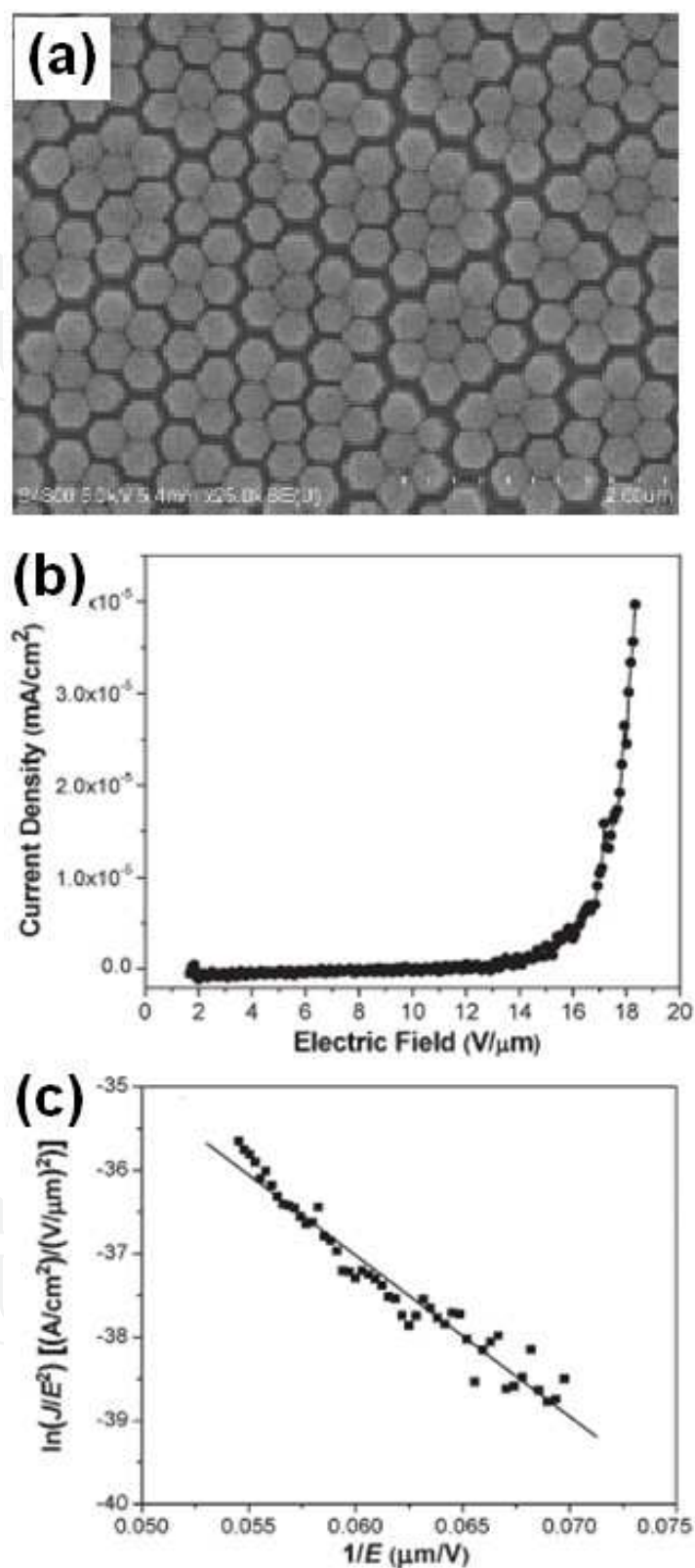
Fig. 34. Top aggregation of a TiO$_2$ nanorod array obtained PLD assisted colloidal lithography with a longer PLD time (80 min) and subsequent annealing. a) FE-SEM image; b) FE J–E curves measured at an anode–cathode distance of 60 mm for a top-aggregated TiO$_2$ nanorod array; c) Corresponding FN plot.
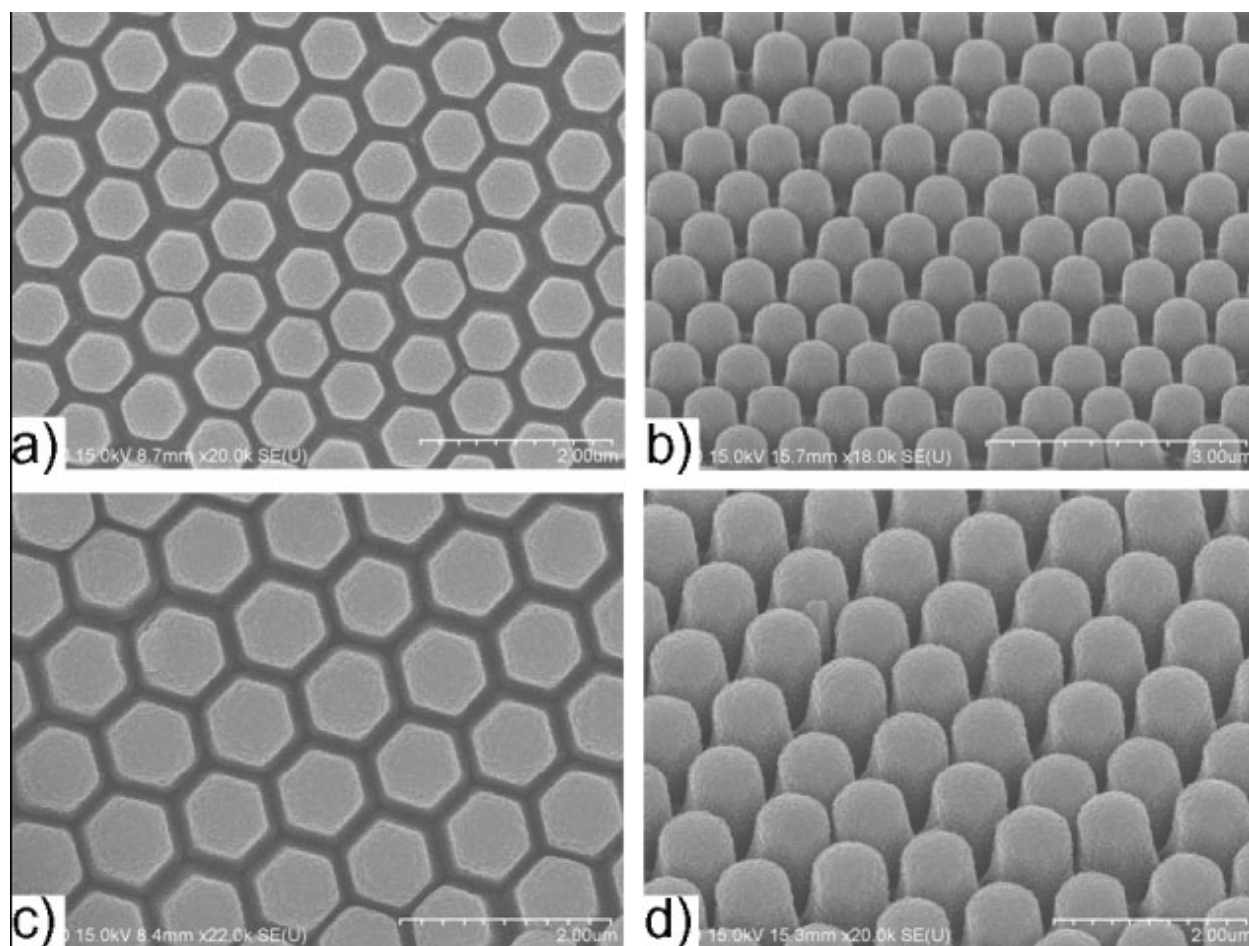
Fig. 35. FE-SEM images of hncp nanorod arrays with different periodicities: 750nm for (a) and (b); 1μm for (c) and (d). PLD was performed in 6.7 Pa of oxygen for 130 min. (a) and (c) are observed from the top, (b) and (d) are observed with a tilt angle of 458.

While a distance between neighboring nanorods can be tuned by changing the background gas pressure during the PLD process if periodicity is fixed to 350 nm for a nanorod array (Figure 22). With increasing this distance of neighboring ones, the field-enhancement factor increased and the turn-on field decreased (Figure 36a). The sample with a small nanorod distance of 20 nm exhibited a relatively low field-enhancement factor of 5.04×10^2 and a high turn-on field of 9.7 V μm^{-1}. When the nanorod distance increased to 50 nm, the FE properties showed enhanced performance with a high field-enhancement factor of 8.38×10^2 and a low turn-on field of 5.6 V μm^{-1}. When the nanorod distance further increased to 110 nm, the best FE properties with a field-enhancement factor of 9.39×10^2 and a turn-on field of 5.3 V μm^{-1} were obtained. (Figure 36b) The above results suggest that optimized FE properties can be achieved by increasing the nanorod distance by controlling the experimental parameters. The increased field-enhancement factor b with the increase of nanorod distance can easily be understood as follows if the periodicity of hncp nanorod array is fixed. The field enhancement factor β is generally related to geometry of an emitter and can be expressed as $\beta \propto h/r$, where h is the height and r is the curvature radius of an emitting center. With an increase in the nanorod distance, the effective diameter of an individual nanorod and a curvature radius r would decrease (Figure 37), resulting in an increase of β according to the above relationship.
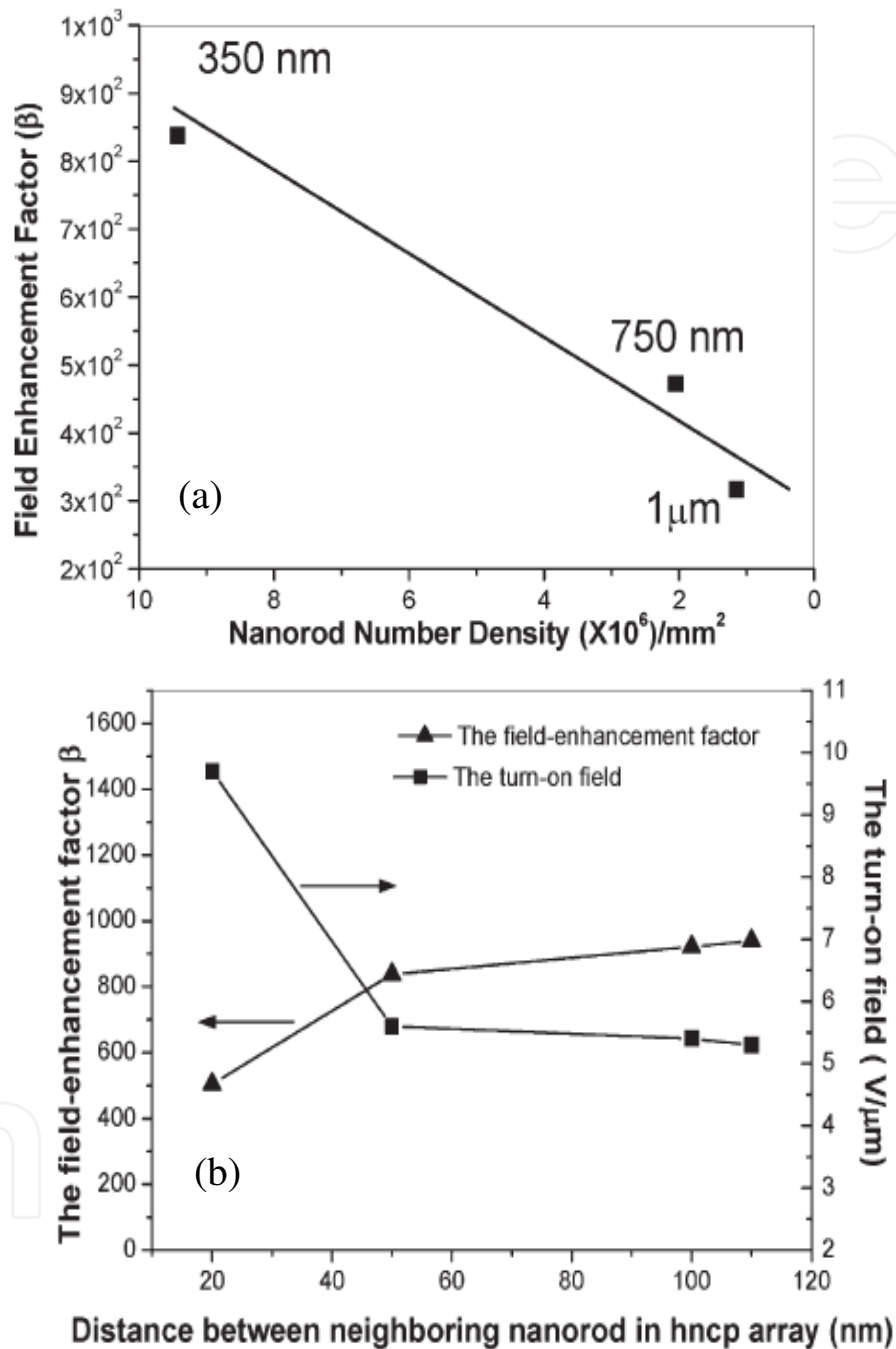
Fig. 36. (a) Field-enhancement factor β changing with increasing periodicity of an hncp nanorod array, (b) Change in field-enhancement factor and turn-on field with varying neighboring nanorod distance in an hncp array.
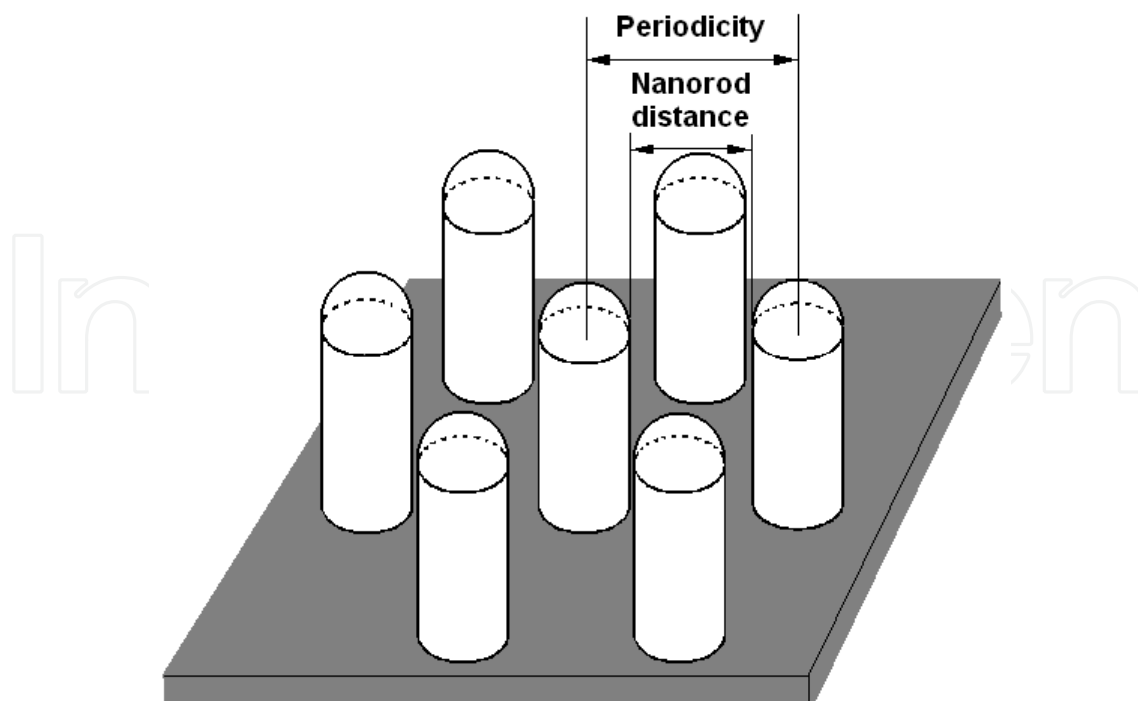
Fig. 37. Schematic illustration of defined nanorod distance in periodic hncp nanorod array.

4.3 Enhanced catalytic properties

The hierarchical micro/nanostructured arrays possess a large specific surface area and hence they might have important application in catalytic fields. For instance, the hcp amorphous TiO_2 micro/nanostructured array on a colloidal monolayer obtained by PLD assisted colloidal lithography demonstrated an enhanced photocatalytic activity (Figure 2). Its photocatalytic performance was estimated based on the decomposition of organic molecules, stearic acid under UV illumination by monitoring the FT-IR spectra.[104,105] The frequencies of 2919 and 2849 cm^{-1} reflect the methylene group asymmetric ($\nu_{asymmCH2}$) and symmetric ($\nu_{symmCH2}$) stretching modes of stearic acid. These values for the methylene group stretching mode are close to those of a crystalline alkane and are typically taken as evidence of the formation of a dense, well-ordered, self-assembled monolayer of stearic acid on the oxide surface.[106-108] Therefore, the photodegradation of stearic acid can be monitor by observing density of these two frequencies. With increasing the UV irradiation time, the vibrational bands of the methylene group gradually decreased and almost completely disappeared after 25 min, as shown in Figure 38a. The decrease in C-H vibrational bands reflects that the stearic acid is gradually photodegraded by such TiO_2 hierarchical micro/nanostructured array films under UV irradiation. Figure 38b shows that degradation curves of a stearic acid film on a silicon wafer, an amorphous TiO_2 film by PLD without using a colloidal monolayer, an hcp amorphous TiO_2 hierarchical micro/nano-rod array on the colloidal monolayer, and an anatase TiO_2 rod array (obtained by annealing hcp amorphous TiO_2 hierarchical micro/nano-rod array on the colloidal monolayer at 650 °C for 2 h. These results indicate that TiO_2 exhibited efficient degradation for stearic acid and that the hcp amorphous TiO_2 hierarchical micro/nano-rod array on a colloidal monolayer demonstrated the best performance compared to the amorphous film and the anatase rod array. Anatase is usually deemed to be more photocatalytically active than the rutile and
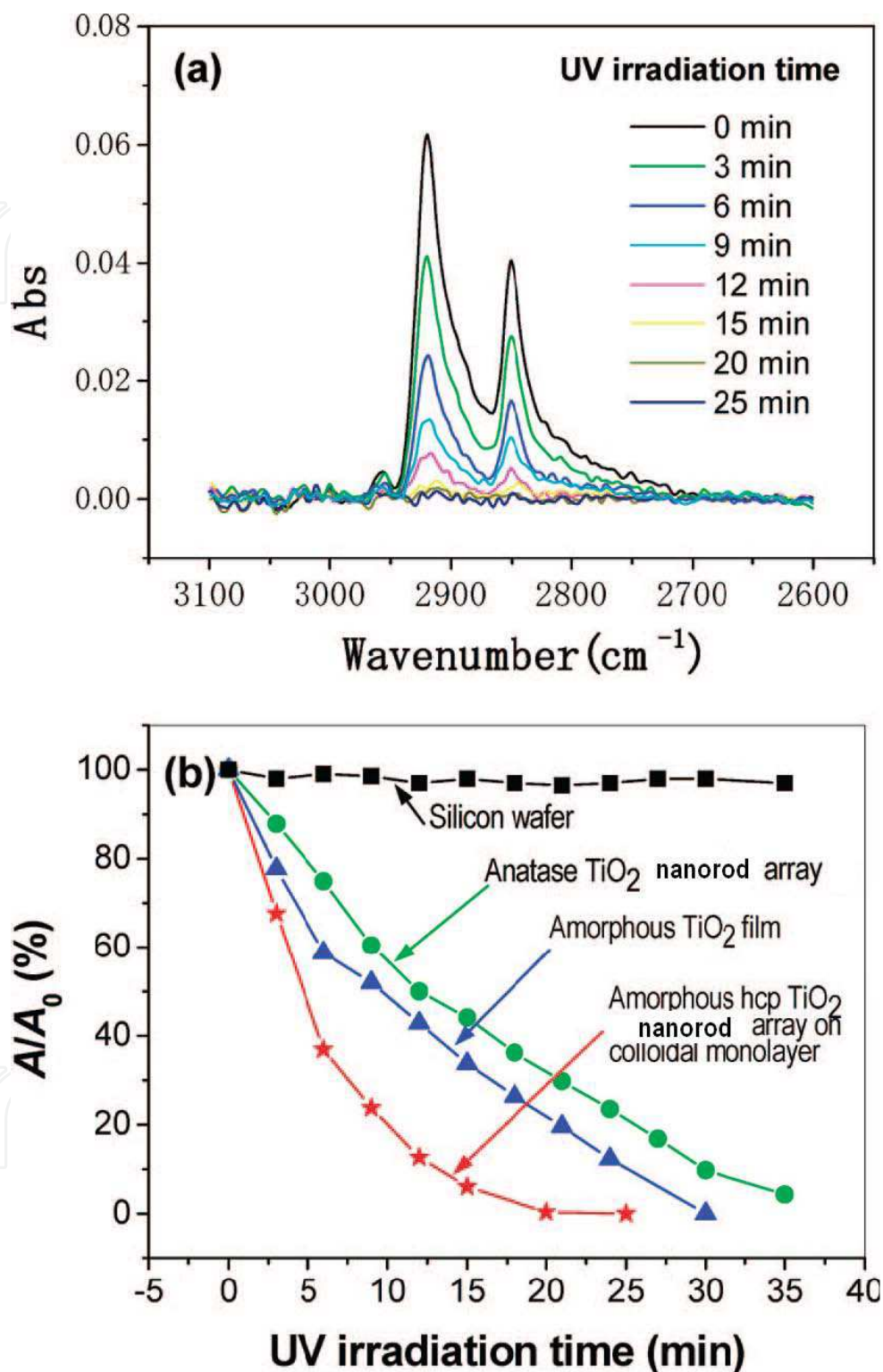
Fig. 38. (a) Photocatalytic activity of an hcp amorphous TiO_2 micro/nano-rod array with a PS colloidal monolayer. (b) Photocatalytic activity evaluation of different substrates based on the absorbance ratio A/A_0 as a function of UV irradiation time. A and A_0 are the absorbance after the UV irradiation and that from the initial surface, respectively.

amorphous TiO_2. However, besides the crystal phase, other factors, including the specific surface area, crystal composition, and material microstructures, also significantly affect the catalytic performance of TiO_2.[109-111] In this case, an amorphous hcp hierarchical micro/nano-rod array has porous structures and possesses a much higher specific surface area than that of an anatase rod array, which contributes to better photocatalytic properties. These results suggest that the surface area of TiO_2 is preferable to its crystal structure for enhancing photocatalytic activity. Additionally, a periodic structured array of amorphous TiO_2 can enhance photocatalytic activity better than an amorphous TiO_2 thin film produced by PLD without using a colloidal monolayer. This may be ascribed to special hierarchical structures composed of radiation-shaped nanobranches emanating from a center point on the PS sphere.[112] The combination of superamphiphilicity and photocatalytic activity is helpful in realizing a self-cleaning surface.
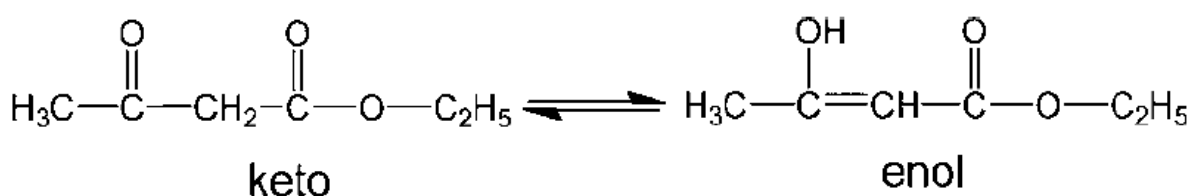

Fig. 39. Isomerization equilibrium of ethyl acetoacetate between the two kinds of isomers, keto and enol.

Additionally, hierarchical alumina mciro/nanostructured arrays demonstrate very excellent catalytic properties for some organic reactions. For example, as we know, ethyl acetoacetate has two kinds of isomers, keto and enol, because of the acidic hydrogen on the active methylene. The corresponding isomerization equilibrium can be depicted in Figure 39. Under common conditions, the keto isomer is more stable than the enol isomer. By the using hierarchical alumina mciro/nanostructured arrays as catalyst, keto isomer might be efficiently converted into the enol isomer. The isomerization can be commonly detected by on-line gas chromatography (GC) or on-line high-performance liquid chromatography (HPLC). Such technique is complicated and, most importantly, not cost-effective. An effective alternative is monitoring the UV-vis spectrum of reaction process. In the keto isomer configuration, there are only two isolated carbonyl groups, with an R absorption band having a quite small ε value in the UV-vis spectrum. For the enol isomer, there is a conjugation system between alkene and carbonyl group, with a K absorption band having a high ε value at around 244 nm in the UV-vis spectrum. This difference makes it convenient to analyze the content and the isomerization process using the UV-vis spectrum. Therefore, the catalytic activity of the hncp alumina was estimated based on the isomerization of ethyl acetoacetate by monitoring the UV-vis absorption spectrum (Figure 40A). The absorption at 244 nm indicates absorption of the conjugation system in the enol isomer as stated above. In the isomerization process, the absorption peak at 244 nm gradually increased and almost completely saturated after 40 min. The increase in absorption at 244 nm indicates that the proportion of enol isomer gradually increased, demonstrating the transition of the keto isomer to the enol isomer and verifying successful isomerization in the presence of hncp alumina. The corresponding control experiments were performed in order to confirm the
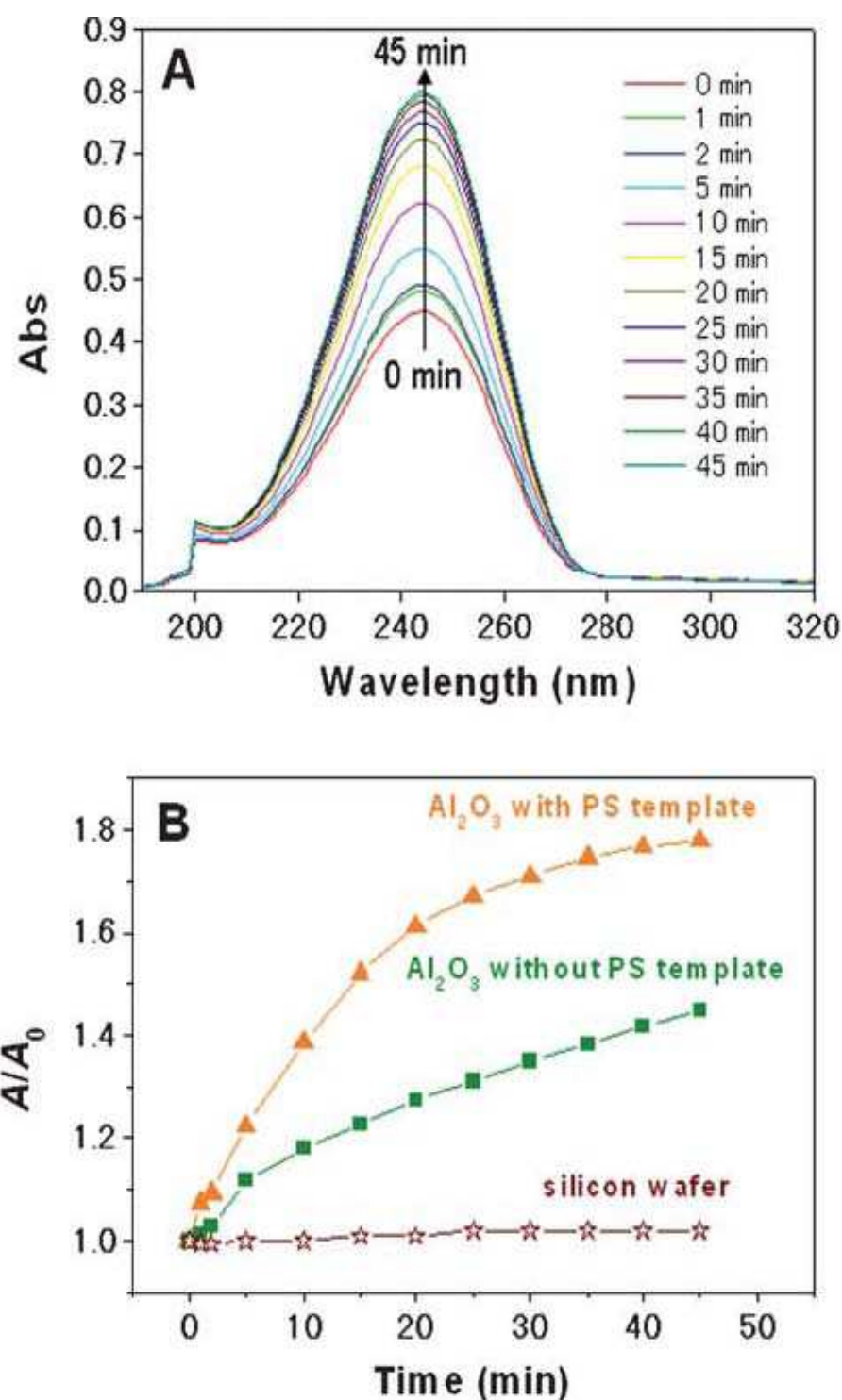
Fig. 40. (A) Catalytic activity of hncp Al_2O_3. (B) Catalytic activity evaluation of different substrates based on the absorbance ratio A/A_0 as a function of reaction time. A and A_0 are the absorbance after a given reaction time and that from the initial solution.

catalytic performance of the hncp alumina for such isomerization. Figure. 40B presents the isomerization process of ethyl acetoacetate in the presence of a silicon wafer and alumina film (by sputtering without using a colloidal monolayer) under the same deposition condition. These results indicate that the hncp alumina exhibited efficient catalytic activity

for the isomerization of ethyl acetoacetate. γ-Alumina is generally deemed to be catalytically active. However, besides the crystal phase, other factors, including the specific surface area, crystal composition, material microstructures, and the absence of exotic species from the remnant starting materials, also significantly affect the catalytic performance.[113-116] In this case, the special hierarchical structures of the amorphous hncp alumina array have porous structures and possess a much higher specific surface area than the dense alumina film, which, together with the pure compositions, contributes to better catalytic properties.

5. Conclusions and remarks

The physical deposition assisted colloidal lithography has proven to be a facile, inexpensive, versatile route to construct hierarchical micro/nanostructured arrays with controlled morphologies, sizes, periodicities. The morphologies of these hierarchical micro/nanostructured arrays can be tuned by controlling the experimental conditions, including deposition time, background gas pressure in the vacuum chamber, periodicity of colloidal monolayer template etc. Compared with chemical routes, the physical deposition are more suitable for preparing high quality micro/nanostructured arrays with uniform morphologies. These special structures possess morphology- or size-dependent properties, such as superamphiphilicity, superhydrophobicity, photocatalytic activity, field emission etc., which have important applications in devices, microfluidic devices, field emitters, solar cells etc. Compared to development of fabrication strategies of micro/nanostructured arrays, investigation of morphology- or parameter- properties and micro/nanodevices dependent on them is not so much. The more micro/nanodevices based on these structures will be hoped, and it might be realized under researchers` efforts in the future.

6. Acknowledgements

7. References

[1] M. Morariu, N. Voicu, E. Schäffer, Z. Lin, T. P. Russell, U. Steiner, *Nat. Mater,.* 2003, 2, 48.
[2] C. H. Ye, L. D. Zhang, X. S. Fang, Y. H. Wang, P. Yan, J. W. Zhao, *Adv. Mater.,* 2004, 16, 1019.
[3] S. V.Dorozhkin, *J. Mater. Sci.: Mater. Med.,* 2007, 18, 363.
[4] G. Duan, W. Cai,Y. Luo, Y. Li, Y. Lei, *Appl. Phys. Lett.,* 2006, 89, 181918.
[5] J. Y. Lao, J. G. Wen, D. Z. Wang, Z. F. Ren, *Nano. Lett.,* 2002, 2, 1287.
[6] P. X. Gao, Y. Ding, Z. L. Wang, *Nano. Lett.,* 2003, 3, 1315.
[7] R. Yan, D. Gargas, P. Yang, *Nat. Photonics,* 2009, 3, 569.
[8] E. Roduner, *Chem. Soc. Rev.,* 2006, 35, 583.
[9] C. M. Cobley, J. Chen, E. C. Cho, L. V. Wang, Y. Xia, *Chem. Soc. Rev.,* 2011, 40, 44.
[10] Z. L., Wang, *Adv. Func Mater.,* 2008, 18, 3553.
[11] R. A. Varin, L. Zbroniec, M. Polanski, J. Bystrzycki, *Energies,* 2011, 4, 1.
[12] Smith, H. I.; Schattenburg, M. L. *IBM J. Res. DeV.* 1993, 37, 319.

[13] Stroscio, J. A.; Eigler, D. M. *Science* 1991, *254*, 1319.

[14] Liu, G.-Y.; Xu, S.; Qian, Y. *Acc. Chem. Res.* 2000, *33*, 457.

[15] Piner, R. D.; Zhu, J.; Xu, F.; Hong, S.; Mirkin, C. A. *Science* 1999, *283*, 661.

[16] Xia, Y. N.; Whitesides, G. M. *Langmuir* 1997, *13*, 2059.

[17] Kumar, A.; Whitesides, G. M. *Appl. Phys. Lett.* 1993, *63*, 2002.

[18] Quist, A. P.; Pavlovic, E.; Oscarsson, S. *Anal. Bioanal. Chem.* 2005, *381*,591.

[19] Kim, E.; Xia, Y.; Whitesides, G. M. *Nature* 1995, *376*, 581.

[20] L. Gao, T. J. McCarthy, *Langmuir*, 2006, *22*, 2966.

[21] Micheletto, R.; Fukuda, H.; Ohtsu, M. *Langmuir* 1995, *11*, 3333.

[22]Rakers, S.; Chi, L. F.; Fuchs, H. *Langmuir* 1997, *13*, 7121.

[23] Denkov, N. D.; Velev, O. D.; Kralchevsky, P. A.; Ivanov, I. B.; Yoshimura, H.; Nagayama, K. *Langmuir* 1992, *8*, 3183.

[24] Denkov, N. D.; Velev, O. D.; Kralchevsky, P. A.; Ivanov, I. B.; Yoshimura, H.; Nagayama, K. *Nature* 1993, *361*, 1303.

[25] Hulteen, J. C.; Van Duyne, R. P. *J. Vac. Sci. Technol.* 1995, *13*, 1553.

[26] Ozin, G. A.; Yang, S. M. *Adv. Funct. Mater.* 2001, *11*, 95.

[27] Jiang, P.; McFarland, M. J. *J. Am. Chem. Soc.* 2004, *126*, 13778.

[28] Wang, D.; Möhwald, H. *Adv. Mater.* 2004, *16*, 244.

[29] Mihi, A.; Ocana, M.; Mí guez, H. *Adv. Mater.* 2006, *18*, 2244.

[30] Li, Y.; Cai, W. P.; Duan, G. T.; Sun, F. Q.; Cao, B. Q.; Lu, F. *Mater.Lett.* 2005, *59*, 276.

[31] Antony, S.; Dimitrov, A. S.; Nagayama, K. *Langmuir* 1996, *12*, 1303.

[32] Jiang, P.; Bertone, J. F.; Hwang, K. S.; Colvin, V. L. *Chem. Mater.*1999, *11*, 2132.

[33] Im, S. H.; Kim, M. H.; Park, O. O. *Chem. Mater.* 2003, *15*, 1797.

[34] Kitaev, V.; Ozin, G. A. *Adv. Mater.* 2003, *15*, 75.

[35] Choi, W. M.; Park, O. O. *Nanotechnology* 2006, *17*, 325.

[36] G. Zhang, D. Wang, *Chem. Asian J.,* 2008, 4, 236.

[37] Y. Li, N. Koshizaki, W. Cai, *Coord. Chem. Rev.,* 2010, 255, 357.

[38] Y. Li, W. Cai, G. Duan, *Chem. Mater.,* 2008, 20, 615.

[39] L. Li, T. Zhai, H. Zeng, X. Fang, Y. Bando, D. Golberg. *J. Mater. Chem.,* 2011, 21, 40.

[40] J. Zhang, B. Yang, *Adv. Funct. Mater.,* 2010, 20, 3411.

[41] S.-M. Yang, S.G. Jang, D.-G. Choi, S. Kim, H.K. Yu, *Small*, 2006, 2, 458.

[42] Sun, F.; Cai, W.; Li, Y.; Duan, G.; Nichols, W. T.; Liang, C.; Koshizaki, N.; Fang, Q.; Boyd, I. W. *Appl. Phys. B: Lasers Opt.* 2005, *81*, 765.

[43] Burmeister, F.; Schäfle, C.; Matthes, T.; Böhmisch, M.; Boneberg, J.; Leiderer, P. *Langmuir* 1997, *13*, 2983.

[44] Pacifica, J.; Gómez, D.; Mulvaney, P. *Ad*V. *Mater.* 2005, *17*, 415.

[45] Jensen, T. J.; Duval, M. L.; Kelly, K. L.; Lazarides, A. A.; Schatz, G. C.; Van Duyne, R. P. *J. Phys. Chem. B* 1999, *103*, 9846.

[46] Malinsky, M. D.; Kelly, K. L.; Schatz, G. C.; Van Duyne, R. P. *J. Phys. Chem. B* 2001, *105*, 2343.

[47] Hulteen, J. C.; Treichel, D. A.; Smith, M. T.; Duval, M. L.; Jensen, T. J.; Van Duyne, R. P. *J. Phys. Chem. B* 1999, *103*, 3854.

[48] Tan, B. J. Y.; Sow, C. H.; Koh, T. S.; Chin, K. C.; Wee, A. T. S.; Ong, C. K. *J. Phys. Chem. B* 2005, *109*, 11100.

[49] Sort, J.; Glaczynska, H.; Ebels, U.; Dieny, B.; Miersig, M.; Rybczynski, J. *J. Appl. Phys.* 2004, *95*, 7516.

[50] Sun, F. Q.; Cai, W. P.; Li, Y.; Cao, B. Q.; Lei, Y.; Zhang, L. D. *Adv. Funct. Mater.* 2004, *14*, 283.

[51] Sun, F. Q.; Yu, J. C.; Wang, X. C. *Chem. Mater.* 2006, *18*, 3774.

[52] Li, Y.; Cai, W. P.; Duan, G. T.; Sun, F. Q.; Lu, F. *Appl. Phys. A: Mater. Sci. Process.* 2005, *81*, 269.

[53] Li, Y.; Cai, W. P.; Cao, B. Q.; Duan, G. T.; Li, C. C.; Sun, F. Q.; Zeng, H. B. *J. Mater. Chem.* 2006, *16*, 609.

[54] Sun, F. Q.; Cai, W. P.; Li, Y.; Cao, B. Q.; Lei, Y.; Zhang, L. D. *Mater. Sci. Technol.* 2005, *21*, 500.

[55] Sun, F. Q.; Cai, W. P.; Li, Y.; Jia, L. C.; Lu, F. *Adv. Mater.* 2005, *17*, 2872.

[56] Sun, F. Q.; Cai, W. P.; Li, Y.; Cao, B. Q.; Lu, F.; Duan, G. T.; Zhang, L. D. *Adv. Mater.* 2004, *16*, 1116.

[57] Cao, B. Q.; Cai, W. P.; Sun, F. Q.; Li, Y.; Lei, Y.; Zhang, L. D. *Chem. Commun.* 2004, 1604.

[58] Cao, B. Q.; Sun, F. Q.; Cai, W. P. *Electrochem. Solid-State Lett.* 2005, *8*, G237.

[59] Duan, G. T.; Cai, W. P.; Li, Y.; Li, Z. G.; Cao, B. Q.; Luo, Y. Y. *J. Phys.Chem. B* 2006, *110*, 7184.

[60] Duan, G. T.; Cai, W. P.; Luo, Y. Y.; Sun, F. Q. *Adv. Funct. Mater.* 2007, *17*, 644

[61] Wang, X.; Lao, C.; Graugnard, E.; Summers, C. J.; Wang, Z. L. *Nano Lett.* 2005, *5*, 1784.

[62] Yan, F.; Goedel, W. A. *Nano Lett.* 2004, *4*, 1193.

[63] Duan, G. T.; Cai, W. P.; Luo, Y. Y.; Li, Z. G.; Lei, Y. *J. Phys. Chem.B* 2006, *110*, 15729.

[64] Li, Y.; Cai, W. P.; Duan, G. T.; Cao, B. Q.; Sun, F. Q. *J. Mater. Res.* 2005, *20*, 338.

[65] Venkatesh, S.; Jiang, P. *Langmuir* 2007, *23*, 8231.

[66] Li, Y.; Huang, X. J.; Heo, S. H.; Li, C. C.; Choi, Y. K.; Cai, W. P.; Cho, S. O. *Langmuir* 2007, *23*, 2169.

[67] Huang, X. J.; Li, Y.; Im, H. S.; Yarimaga, O.; Kim, H. J.; Jang, D. Y.; Cho, S. O.; Cai, W. P.; Choi, K. Y. *Nanotechnology* 2006, *17*, 2988.

[68] Correa-Duarte, M. A.; Kosiorek, A.; Kandulski, W.; Giersig, M. *Small* 2006, *2*, 220.

[69] Li, Y.; Lee, E. J.; Cho, S. O. *J. Phys. Chem. C* 2007, *111*, 14813.

[70] Li, Y.; Li, C. C.; Cho, S. O.; Duan, G. T.; Cai, W. P. *Langmuir* 2007, *23*, 9802.

[71] Duan, G. T.; Cai, W. P.; Luo, Y. Y.; Li, Y.; Lei, Y. *Appl. Phys. Lett.* 2006, *89*, 181918.

[72] Qi, L. M.

[73] Li, Y.; Sasaki, T.; Shimizu, Y.; Koshizaki, N. *J. Am. Chem. Soc.* 2008, *130*, 14755.

[74] Li, Y.; Koshizaki, N.; Shimizu, Y.; Li, L.; Gao, S. Sasaki, T. *ACS Appl. Mater. & Interfaces.* 2009, *1*, 2580.

[75] Nam, H. J.; Sasaki, T.; Koshizaki, N. *J. Phys. Chem. B* 2006, *110*, 23081.

[76] Brett, M. J.; Hawkeye, M. M. *Science* 2008, *319*, 1192.

[77] Robbie, K.; Beydaghyan, G.; Brown, T.; Dean, C.; Adams, J.; Buzea, C. *Rev. Sci. Instrum.* 2004, *75*, 1089.

[78] Zhao, Y.-P.; Ye, D.-X.; Wang, G.-C.; Lu, T.-M. *Nano Lett.* 2002, *2*, 351.

[79] Hrudey, P. C. P.; Szeto, B.; Brett, M. J. *Appl. Phys. Lett.* 2006, *88*, 251106.

[80] Kesapragada, S. V.; Victor, P.; Nalamasu, O.; Gall, D. *Nano Lett.* 2006, *6*, 854.

[81] He, Y. P.; Fu, J. X.; Zhang, Y.; Zhao, Y. P.; Zhang, L. J.; Xia, A. L.; Cai, J. W. *Small* 2007, *3*, 153.

[82] Zhou, C. M.; Gall, D. *Appl. Phys. Lett.* 2006, *88*, 203117.

[83] Robbie, K.; Sit, J. C.; Brett, M. J. *J. Vac. Sci. Technol., B: Microelectron. Nanometer Struct.sProcess., Meas., Phenom.* 1998, *16*, 1115.

[84] Vick, D.; Tsui, Y. Y.; Brett, M. J.; Fedosejevs, R. *Thin Solid Films* 1999, *350*, 49.

[85] Li, Y.; Sasaki, T.; Shimizu, Y.; Koshizaki, N. Small, 2008, 4, 2286.

[86] Li, Y.; Fang, X.; Koshizaki, N.; Sasaki, T.; Li, L.; Gao, S.; Shimizu, Y.; Sasaki, T.; Bando, Y.; Golberg, M. Adv. Funct. Mater. 2008, 19, 2467.

[87] Li, L.; Koshizaki, N. J. Mater. Chem., 2010, 20, 2972

[88] Li, L.; Li, Y.; Gao, S.; Koshizaki, N. J. Mater. Chem., 2009, 19, 8366.

[89] Gao, S.; Koshizaki, N.; Li, Y.; Li, L. J. Mater. Chem., 2011, 21, 2087.

[90] A. Nakajima, K. Hashimoto, T. Watanabe, Monatsh. Chem. 132 (2001) 31.

[91] T. Sun, L. Feng, X. Gao, L. Jiang, Acc. Chem. Res. 38 (2005) 644.

[92] X.-M. Li, D. Reinhoudt, M. Crego-Calama, Chem. Soc. Rev. 36 (2007) 1350.

[93] X.-J. Huang, J.-H. Lee, J.-W. Lee, J.-B. Yoon, Y.-K. Choi, Small 4 (2008) 211.

[94] X.-J. Huang, D.-H. Kim, M. Im, J.-H. Lee, J.-B. Yoon, Y.-K. Choi, Small, 2008, 5, 90

[95] R.N. Wenzel, J. Phys. Colloid Chem. 1949, 53, 1446.

[96] R. Wang, K. Hashimoto, A. Fujishima, M. Chikuni, E. Kojima, A. Kitamura, M. Shimohigoshi, T. Watanabe, Adv. Mater. 1998, 10, 135.

[97] W.-L. Min, B. Jiang, P. Jiang, Adv. Mater. 2008, 20, 3914.

[98] Y. Li, J. Zhang, S. Zhu, H. Dong, Z. Wang, Z. Sun, J. Guo, B. Yang, J. Mater. Chem. 2009, 19, 1806.

[99] Y.-R. Lin, H.-P. Wang, C.-A. Lin, J.-H. Hea, J. Appl. Phys. 2009, 106, 114310.

[100] A. Cassie and S. Baxter, Trans. Faraday Soc., 1944, 40, 546.

[101] S.S. Fan, M.G. Chapline, N.R. Franklin, T.W. Tombler, A.M. Cassell, H.J. Dai, Science 283 (1999) 512.

[102] X.S. Fang, Y. Bando, U.K. Gautam, C.H. Ye, D. Golberg, J. Mater. Chem. 18 (2008) 509.

[103] R.H. Fowler, L.W. Nordheim, Proc. R. Soc. London, Ser. A 119 (1928) 173.

[104] Wang, K. X.; Yao, B. D.; Morris, M. A.; Holmes, J. D. *Chem. Mater.* 2005, *17*, 4825.

[105] Zhang, X. T.; Jin, M.; Liu, Z. Y.; Tryk, D. A.; Nishimoto, S.; Murakami, T.; Fujishima, A. *J. Phys. Chem. C* 2007, *111*, 14521.

[106] Gao, W.; Dickinson, L.; Grozinger, C.; Morin, F. G.; Reven, L. *Langmuir* 1996, *12*, 6429.

[107] Nuzzo, R. G.; Dubois, L. H.; Allara, D. L. *J. Am. Chem. Soc.* 1990, *112*, 558.

[108] Gawalt, E. S.; Avaltroni, M. J.; Koch, N.; Schwartz, J. *Langmuir* 2001, *17*, 5736.

[109] Fujishima, A.; Zhang, X. T. *C. R. Chimie* 2006, *9*, 750.

[110] Macak, J. M.; Zlamal, M.; Krysa, J.; Schmuki, P. *Small* 2007, *3*, 300.

[111] Wu, C. Z.; Lei, L. Y.; Zhu, X.; Yang, J. L.; Xie, Y. *Small* 2007, *3*, 1518.

[112] Li, H. X.; Bian, Z. F.; Zhu, J.; Zhang, D. Q.; Li, G. S.; Huo, Y. N.; Li, H.; Lu, Y. F. *J. Am. Chem. Soc.* 2007, *129*, 8406.

[113] J. Li, R. Yan, B. Xiao, D. T. Liang and L. Du, Environ. Sci. Technol., 2008, 42, 6224;

[114] L. B. Sun, J. Yang, J. H. Kou, F. N. Gu, Y. Chun, Y. Wang, J. H. Zhu and Z. G. Zou, Angew. Chem., Int. Ed., 2008, 47, 3418;

[115] C. Misra, American Chemical Society Monograph, in Industrial Alumina Chemicals, American Chemical Society, Washington, DC,1986, vol. 184;

[116] B. R. Baker and R. M. Pearson, J. Catal., 1974, 33, 265.
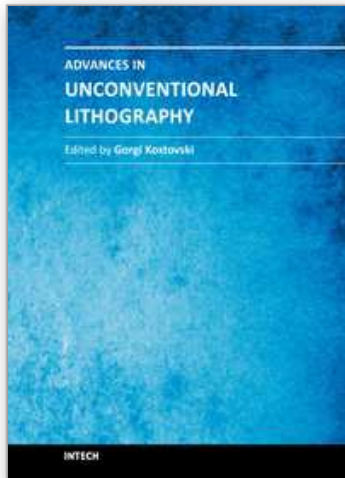
Advances in Unconventional Lithography
Edited by Dr. Gorgi Kostovski

The term Lithography encompasses a range of contemporary technologies for micro and nano scale fabrication. Originally driven by the evolution of the semiconductor industry, lithography has grown from its optical origins to demonstrate increasingly fine resolution and to permeate fields as diverse as photonics and biology. Today, greater flexibility and affordability are demanded from lithography more than ever before. Diverse needs across many disciplines have produced a multitude of innovative new lithography techniques. This book, which is the final instalment in a series of three, provides a compelling overview of some of the recent advances in lithography, as recounted by the researchers themselves. Topics discussed include nanoimprinting for plasmonic biosensing, soft lithography for neurobiology and stem cell differentiation, colloidal substrates for two-tier self-assembled nanostructures, tuneable diffractive elements using photochromic polymers, and extreme-UV lithography.

INTECH
open science | open minds